Journal of
Marine Science and Engineering

Article

Modeling and Simulation of a Turbine Access System with Three-Axial Active Motion Compensation

Jingfu Wang [1], Songtao Zhang [1,*], Jiahuan Cheng [2], Yunfei Li [1,*], Yan Shen [1] and Zihao Wu [1]

[1] College of Intelligent Systems Science and Engineering, Harbin Engineering University, Harbin 150001, China; ahwjf@hrbeu.edu.cn (J.W.); shenyan0715@163.com (Y.S.); xiaocuihuaer@163.com (Z.W.)
[2] China Ship Development and Design Center, Shanghai 201108, China; cjh198808@163.com
* Correspondence: hrbzst@126.com (S.Z.); liyunfei@hrbeu.edu.cn (Y.L.); Tel.: +86-139-4603-2279 (S.Z.); +86-176-3486-6593 (Y.L.)

Abstract: As an essential transportation equipment for personnel to access offshore wind plants, the safety and stability of the turbine access system (TAS) have gained increasing significance. However, when sea conditions deteriorate, the end of the TAS will experience large-angle shaking and an increase in the heave height. A novel 3-DOFs TAS with active motion compensation for the Fujian coastal area is designed to solve the problem of the stability of the end of the TAS under sea conditions with a significant wave height of 2.2 m, including structural design, kinematic analysis, hydraulic drive design, and control system design. In the research, a new stacking compensation method is proposed to compensate for the roll angle, pitch angle, and heave height at the end of the TAS. The 3-DOFs TAS is modeled mathematically by the Denavit–Hartenberg parameters, and the hydraulic system model is established. In order to improve the compensation effect, a fuzzy PID controller with feedforward compensation is designed based on fuzzy PID control, and the model simulation experiment is carried out by MATLAB/Simulink. Finally, the experimental simulation shows that under the compensation of the feedforward compensation fuzzy PID control algorithm and the new compensation algorithm, the roll angle of the TAS is reduced by a maximum of 84.8%, the pitch angle is reduced by 75%, and the heave height is reduced by 73.6%. This validates the effectiveness of the proposed scheme and provides a reference for future TAS design and development.

Keywords: active motion compensation; turbine access system; kinematic analysis; fuzzy PID control; offshore wind plants

Citation: Wang, J.; Zhang, S.; Cheng, J.; Li, Y.; Shen, Y.; Wu, Z. Modeling and Simulation of a Turbine Access System with Three-Axial Active Motion Compensation. *J. Mar. Sci. Eng.* **2023**, *11*, 2237. https://doi.org/10.3390/jmse11122237

Academic Editor: José-Santos López-Gutiérrez

Received: 24 October 2023
Revised: 15 November 2023
Accepted: 22 November 2023
Published: 26 November 2023

1. Introduction

In the context of the growing tension surrounding land resources, a rising awareness has emerged regarding the abundant resources of the ocean. Offshore wind plants present several advantages over land-based wind plants, such as a smaller land use area and more abundant wind resources [1]. In 2021, China added 16.9 million kilowatts of wind turbines, which is 1.8 times as many as all other wind turbines built before. Some scholars have even proposed new hybrid devices that can capture wind and wave energy and proposed new optimization solutions [2]. However, the harsh marine environment poses a threat to the safety of maritime operators, mainly due to the roll, pitch, yaw, sway, surge, and heave caused by waves [3]. Therefore, this requires the turbine access system (TAS) to transport operators and various equipment from ships to wind turbines. This not only improves the safety of offshore operators and reduces the difficulty of offshore operations, but also improves the efficiency of offshore operations [4].

In the offshore industry, two means of transport are being used to reach offshore structures: helicopters and vessels [5].

1. Helicopter access. Helicopters have higher safety and commuting efficiency and are mainly used for the operation and maintenance of large wind farms. Helicopter

transportation and transfer are not limited by wave conditions. China's offshore wind power plants are built on the continental shelf, usually 10–20 km away from the coast, while in some European countries, such as the Netherlands, offshore wind power plants can reach a distance of 30–100 km [6]. Taking an offshore wind farm 100 km offshore as an example, the average maximum speed of crew transfer vehicles (CTVs) is 25 knots, which can be reached by boat in 2.2 h, while it only takes half an hour by helicopter [7]. However, there are limitations to the use of helicopters. It is required to install a platform on the wind turbine for helicopters and personnel to use. Although this method is fast, its drawbacks are high operating costs and the need for a lifting platform for each turbine. In addition, it is not suitable for situations with high winds or low visibility, which can easily lead to accidents. Although the probability of helicopter crashes is low, the likelihood of such accidents causing a large number of deaths is high.

2. Ship-based access. In oil and gas extraction, personnel are generally transported through personnel baskets and swing ropes. Both methods have a major drawback, which is that in order to ensure personnel safety, they must be transported under relatively mild sea conditions. Both methods require the ship to be equipped with a crane, which transports personnel to the target working point through its long boom and cable. However, once encountering wind and waves that cause the ship to sway, the long boom of the crane will have a strong amplification effect, causing severe shaking at the end of the boom and cable. This poses a serious threat to the safety of personnel. Due to unpredictable wind and wave conditions, offshore lifting operations are difficult. Performing lifting operations typically requires special, expensive, and scarce equipment [5,8]. In addition, the ship is propelled forward through the propeller to increase friction between the bow rubber buffer and the landing point, which can eliminate the effects of sway and yaw. The DP system (dynamic positioning system) can effectively suppress the sway and surge of the ship's hull, which can reduce the impact of waves on the ship. However, an important drawback of this access method is that it is only limited to medium wave conditions [9]. Considering safety and cost-effectiveness issues, the offshore wind power industry is not keen on using helicopters as the main access method for offshore wind turbines, and ships have become the most commonly used vehicles.

After determining the vehicle, it is necessary to determine the method to compensate for interference caused by waves, which requires the use of active motion compensation technology to achieve appropriate compensation. The research on motion compensation technology originated from the needs of offshore drilling, and later evolved into various compensation methods, such as velocity compensation, displacement compensation, force compensation, and comprehensive compensation [10]. Taking seabed salvage, recovery, and rescue operations as an example, Southland outlined the difficulties of handling heavy objects at sea and proposed, for the first time, the use of active and passive compensation systems to address interference caused by wind and waves [11].

In current offshore operations, whether using the TAS or other offshore tools, such as offshore cranes, the heave effect is the most affected. Therefore, researchers have conducted extensive research on the heaving effect of waves. In order to reduce the impact of heave motion on the launch and recovery of remotely operated vehicles (ROVs), Yang et al. [12] designed an active heave compensation system mainly based on hydraulic winches, which reduces the impact of the heave motion of the tether management system (TMS) on remote-controlled submersibles by controlling the extension and contraction of the cable. Sebastian et al. [13] proposed an active compensation control algorithm to control hydraulic-driven winches, which considers the delay between the length of the winch rope and the payload to compensate for the vertical motion of the ship. Huang et al. [14] used the Lagrange kinematics equation and numerical simulation to analyze the influence of the rope length and lifting speed of the floating crane wave compensation system on the system response, which has great reference significance for the design of wave compensation systems. Zhou et al. [15] proposed a genetic PID (proportional-integral-differential) controller with feedforward compensation for compensating cranes to optimize the optimal indicators and PID parameters of the system. While maintaining system stability and accuracy, it improved the system's fast response ability and achieved good control results. Xie et al. [16] proposed an active heave compensation method of an electric marine winch based on the sliding-mode control algorithm to solve the six degrees of freedom of the mother ship caused by wave fluctuations and achieved excellent results.

The research on the TAS based on wave compensation has also made significant progress. Christopher put forward the earliest concept of the gangway, which includes a support frame designed to be supported by grating positioned above horizontal structural members of the offshore structure. It mainly provides access in environments seriously affected by weather conditions [17]. There are many factors that affect the compensation effect of TAS, such as model complexity, control strategies, and structural design. For model complexity, Rong et al. proposed a discrete time transfer matrix method of a multibody system for dynamic modeling and analysis of a ship's seaborne supply (SSS) systems, which is used to solve real-time dynamic analysis of SSS operations under complex sea conditions [18]. The method can easily solve the dynamic problems of the system by only using low-order transfer equations, which have lower computational complexity and a satisfactory compensation effect. For control algorithms, Tang et al. established and simulated the wave compensation control model using particle swarm optimization (PSO) to optimize the control parameters of the controller. The result showed that this design has the optimization effects of small over-shoot and a fast response time [19]. Cai et al. proposed a sliding-mode control scheme for the ship-mounted Stewart platform to increase the workable time of carrying out these operations of offshore installations [20]. The novel velocity feedforward compensator and command-filtered-based sliding-mode backstepping controller have been proposed and used on this platform, demonstrating good compensation performance. Yin et al. proposed a novel Stewart platform with a gangway, which is equipped with a robust controller and an estimator [21]. This ensures that the control force does not increase indefinitely with position and attitude errors. The simulation results verified the effectiveness and performance of the controller. Chen proposed a three-loop control strategy based on active disturbance rejection control (ADRC), in which the internal model controller (IMC) in the current loop is designed to achieve fast control. This method has excellent performance in reducing power consumption, decoupling control, and anti-interference [22]. Zhang et al. proposed a system method for designing multivariable fuzzy logic controllers, which applies genetic algorithms to optimize fuzzy scaling factors and can reject strong disturbances [23]. Bai et al. proposed a kinematic-based Lagrangian method for generating motion equations and designing adaptive control laws for multi-body systems based on the dynamic analysis and controller design of the Stewart platform. This method can tolerate performance under large parameter errors and external interference [24]. Liu et al. designed an improved adaptive control strategy based on a radial basis function neural network (RBFNN) with fading factors to compensate for external interference on the Stewart platform. This method reduced the error by 70% and the heave compensation error by 40% [25].

For structural renovation, Chen et al. proposed a new turbine access system suitable for the Taiwan Strait [26]. This design effectively reduced the roll angle, vertical displacement, and vertical acceleration. However, the design is only suitable for marine environments with a significant wave height of 1.5 m. Huang et al. added a fourth axis mechanism to the 3-DOFs TAS, proposing a four-axis TAS to compensate for the surge displacement, heave displacement, pitch angle, and roll angle of the end effector under wave conditions and load tests in the Taiwan Strait. This study used a model reference robust adaptive controller (MRRAC) for control [27]. Tang et al. proposed a four degrees of freedom rope-driven, rigid, flexible hybrid wave compensation mechanism. This wave compensation device can achieve compensation for four degrees of freedom: heave, sway, roll, and pitch, by controlling the mobile platform, reducing, or even eliminating, the relative motion of the ship [28]. In addition, some commercial companies have also launched motion compensation systems for offshore wind power plants. The company Ampelmann launched the first 6-DOFs TAS Stewart, which measures the motion state of the ship in real time through sensors [29]. Nonetheless, the device was constructed using a platform featuring six hydraulic cylinders, resulting in a structurally intricate design that necessitates a substantial amount of space. The company Houlder (London, UK) has developed a kind of TAS, which can compensate for roll, pitch, and surge, but cannot achieve full compensation [30].

This study focuses on reducing the end-angle shaking and vertical height increase of the TAS under adverse sea conditions, and proposes a novel TAS designed for the coastal area of Fujian, which addresses the challenge of maintaining the stability of the TAS in the presence of sea conditions characterized by significant wave heights of up to 2.2 m. A new stacking compensation method is proposed to compensate for the roll angle, pitch angle, and heave height at the end of the TAS. The effects of ship roll, pitch, and heave on the end of the TAS are analyzed separately and compensation values are calculated. The sum of the compensation values is used as the final compensation value for the TAS. In addition, the mathematical modeling of a 3-DOFs TAS and hydraulic system is conducted using the D-H modeling method. A fuzzy PID controller with feedforward for the TAS is developed based on fuzzy PID control theory. The model simulation experiments are then performed using MATLAB/Simulink. Finally, the simulation shows that compared to PID controllers, the control strategy proposed in this study can reduce the roll angle, pitch angle, and heave height of the TAS by 84.8%, 75%, and 73.6%, respectively. The displacement of the TAS end in the X, Y, and Z axes is reduced by at least 65%, with a maximum reduction of 82.69%.

2. Mechanical Structure Design of the TAS

The design proposed in this study solely accounts for the influence of roll, pitch, yaw, and heave on the ship, as it is assumed that the vessel will be outfitted with a DP system.

Based on the above considerations, a TAS with three degrees of freedom active motion compensation, including a rotary joint, pitch joint, and telescopic joint, was designed. The mechanical structure and dimensions of the TAS are shown in Figure 1. The rotary joint contains a symmetrical hydraulic cylinder, the pitch joint contains two asymmetrical hydraulic cylinders, and the telescopic joint contains one asymmetrical hydraulic cylinder. As roll, pitch, and yaw represent rotational movements, the end effector of the TAS may produce varied movements in distinct dimensions, necessitating coordinated movements among different joints for compensation. Specifically, to effectively compensate for roll motion, the pitch and telescopic joints must cooperate, while other joints may need to collaborate to address pitch and yaw movements, and so on. In addition, there is a ladder at the back of the TAS for people to pass, and there is an aluminum alloy guardrail at the top to protect the workers' safety.

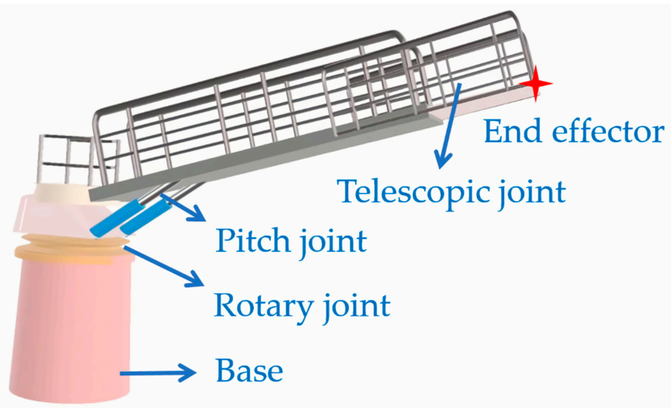

Figure 1. Mechanical structure of the TAS.

3. Ship Motion Model

In order to obtain motion of the TAS, it is necessary to obtain the motion of the ship when it is disturbed by sea waves. Therefore, modeling of random sea waves and ship motions must be carried out.

3.1. Wave Model

It is difficult to calculate the complex and irregular wave motion. However, it is generally believed that when studying the effect of sea waves on ships, the sea waves are regarded as a stationary random process [31]. The power spectral density of waves is a crucial aspect of ocean wave models, as it illustrates the distribution of wave energy across different frequencies. Now, Pierson–Moskowitz and JONSWAP spectra are extensively employed in oceanographic research because they can describe wave motion in most sea areas.

However, the wave motion in different sea areas is different. This study focuses on the coastal region of Fujian Province and adopts the Putian spectrum derived by Yang et al. [32] from the statistical analysis of the nearby sea area of Putian City, Fujian Province. It can be described as:

$$\frac{S(\omega/\overline{\omega})}{M_0} = 1.8865\left(\frac{\omega}{\overline{\omega}}\right)^{-4.5} \exp\left[-0.9632\left(\frac{\omega}{\overline{\omega}}\right)^{-2.8}\right] \times \left[1 + 0.4334\left(\frac{\omega}{\overline{\omega}}\right)^{-2.8}\right] \tag{1}$$

$$H_{1/3} = 3.75\sqrt{M_0} \tag{2}$$

where ω is the wave frequency, $\overline{\omega}$ is the average wave frequency, M_0 is the zero-order moment of the power spectral density of the wave, and $H_{1/3}$ is the significant wave height.

The sea wave can be seen as a superposition of countless harmonic components with different frequencies and phases [33]. These tiny cosines have random initial phases, which is noteworthy. Assuming the existence of the ground coordinate system, $E - \xi\eta\varsigma$, the ship coordinate system, $O - xyz$, the $E - \xi\eta$ plane parallel to the Ox axis, and the angle between the Ox axis and the $E\xi$ axis is μ, the wave height can be described as:

$$\zeta(t) = \sum_{i=1}^{\infty} \zeta_{ai} \cos(k_i\xi \cos\mu + k_i\eta \sin\mu - \omega_i t + \varepsilon_i) \tag{3}$$

where ζ_{ai} is the amplitude of the i-th harmonic component, k_i is the wave number of the i-th harmonic component, ω_i is the angular frequency of the i-th harmonic component, and ε_i is the initial phase of the i-th harmonic component.

According to the statistical results of Jian Shi et al. [34] on the sea wave data along the coast of China from 1979 to 2017, the mean significant wave height and mean period in the four seasons near Putian City, Fujian Province, from 1979 to 2017 are shown in Table 1.

Table 1. The mean significant wave height and mean period of the coast of Putian City during the four seasons from 1979 to 2017.

Season	Mean Significant Wave Height (m)	Mean Period (s)
Spring	1.5	5.3
Summer	1.2	5.7
Autumn	2.2	6.8
Winter	2.5	6.5

According to Table 1, it can be calculated that the mean significant wave height within a year is 1.85 m, and the mean wave period within a year is 6.075 s. Therefore, the mean period of waves in this paper was set to 6 s. Due to the significant differences in the height of meaningful waves in different seasons along the coast of Putian, in order to ensure that the TAS can be used for most of the year, the maximum significant wave height of the usage environment was set to 2.2 m.

From Figure 2a, the frequency of the energy spectrum concentration of waves ranges from 0.5 rad/s to 3.5 rad/s, and the peak frequency of the spectrum is around 0.8 rad/s, which is not consistent with the mean frequency. This is normal because the peak frequency is indeed related to the average frequency of waves, but it is not always the same. From Figure 2b, the amplitude of the wave is between 0 m and 3.5 m, and the first one-third of the amplitude height is concentrated between 1.8 m and 3.5 m, which is consistent with the significant wave height of 2.2 m.

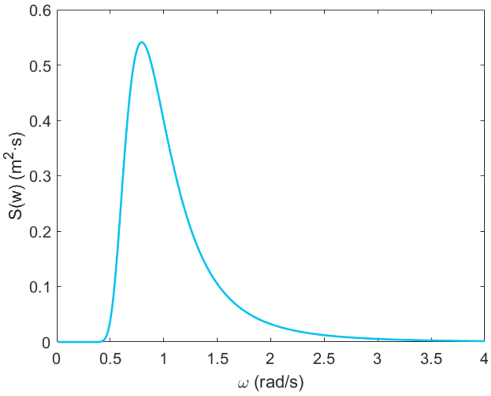

(**a**)

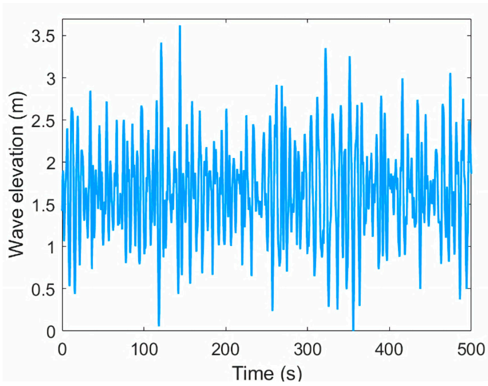

(**b**)

Figure 2. Wave simulation: (**a**) power spectral density of the wave and (**b**) height of the wave.

For the calculation of peak frequency, the peak frequency is the frequency at spectral density, indicating that the most wave energy is concentrated at this frequency. The average frequency is the average of all frequencies, weighted by their respective spectral density values. The average frequency of the waves in Figure 2a can be obtained by the following equation:

$$\begin{cases} S(\omega_i)_{total} = \sum\limits_{i=1}^{n} S(\omega_i) \\ \omega_0 = \sum\limits_{i=1}^{n} \frac{\omega_i S(\omega_i)}{S(\omega_i)_{total}} \end{cases} \tag{4}$$

where ω_0 is the peak frequency, $S(\omega_i)$ is the power spectrum of ω_i, and $S(\omega_i)_{total}$ is the total power spectrum.

According to Equation (4), the average wave period of the simulation model ω_0 = 1.0767 rad/s. According to the set period T_0 = 6 s, the set frequency of ocean waves can be calculated as:

$$\omega = \frac{2\pi}{T} = 1.05 \text{ rad}/s \tag{5}$$

This is very similar to the calculation results, ω_0, verifying the correctness of the wave model.

3.2. Model of Ship Motion

The forces and moments acting on the ship are affected by many factors, and can usually be expressed as:

$$F = F_s + F_H + F_P + F_c + F_D \tag{6}$$

$$G = G_s + G_H + G_P + G_c + G_D \tag{7}$$

where F_s and G_s are the restoring force and restoring moment received of the ship, respectively, F_H and G_H are the hydrodynamic force and hydrodynamic moment of the ship, respectively, F_P and G_P are the propeller thrust and thrust moment of the ship, respectively, F_c and G_c are the control force and restraint moment provided by the ship control system, respectively, while F_D and G_D are the disturbing forces and moments generated by the marine environment, respectively.

It can be seen from Equation (3) that the long peak wave is composed of numerous sub-waves, so the interference force and moment of roll, pitch, yaw, and heave on the ship can be described as:

$$R = \sum_{i=1}^{n} R_i \tag{8}$$

$$P = \sum_{i=1}^{n} P_i \tag{9}$$

$$Y = \sum_{i=1}^{n} Y_i \tag{10}$$

$$H = \sum_{i=1}^{n} H_i \tag{11}$$

where R_i is the roll interference force and interference torque of the i-th harmonic component to the ship, P_i is the pitch interference force and interference torque of the i-th harmonic component to the ship, Y_i is the yaw interference force and interference torque of the i-th harmonic component to the ship, and H_i is the heave interference force and interference torque of the i-th harmonic component to the ship.

Based on the above theory, the six degrees of freedom simulation of a supply ship was carried out using the MATLAB MSS (Marine Systems Simulator) toolbox [35]. The parameters of the supply vessel are shown in Table 2.

Table 2. Parameters of the supply vessel.

Parameter	Value
Draught (m)	6.0
Breadth (m)	19.2
Length between perpendiculars (m)	82.8
Mass (kg)	6.3622×10^6
Radius of gyration in roll (m)	6.72
Radius of gyration in pitch (m)	2.70
Radius of gyration in yaw (m)	20.70
Volume displacement (m^3)	6.207×10^3
Transverse metacentric height (m)	2.1140
Lateral metacentric height (m)	103.6280

The simulation conditions were set as follows: the significant wave height was 2.2 m, the mean period was 6 s, the peak frequency was 0.8 rad/s, and the encounter angles were 45 and 90 degrees. The 6-DOFs simulation results of the ship are shown in Figure 3.

From Figure 3a,b, the maximum amplitude of roll is about 2.2 degrees, and the amplitude is constantly changing. The maximum angles of pitch and yaw are 2 and 0.7 degrees, respectively. The maximum displacement of sway and surge is 0.4 m, and the maximum displacement of heave is 0.7 m.

However, the encounter angle can affect the 6-DOFs motion of the ship. From Figure 3c,d, when the encounter angle is 90 degrees, the roll angle significantly increases, with the maximum amplitude approaching 3 degrees. This is because the angle of action of the waves has changed from 45 to 90 degrees, which increases the force on the hull, resulting in an increase in the amplitude of the roll angle. On the contrary, the amplitude of pitch decreases due to a decrease in longitudinal force on the hull. For linear motion, the increase in roll causes an increase in the shaking amplitude of the ship, resulting in an increase in vertical motion displacement, while the rest of the motion changes little.

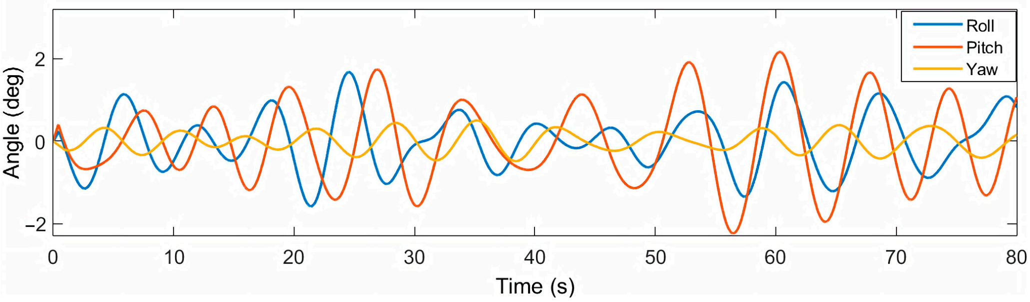

(**a**)

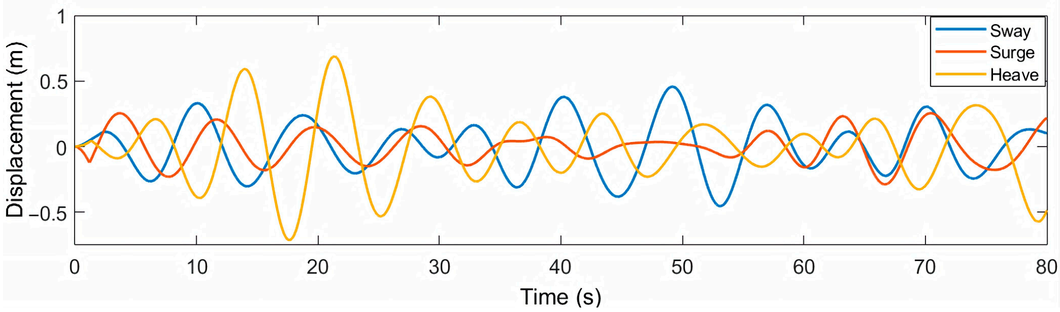

(**b**)

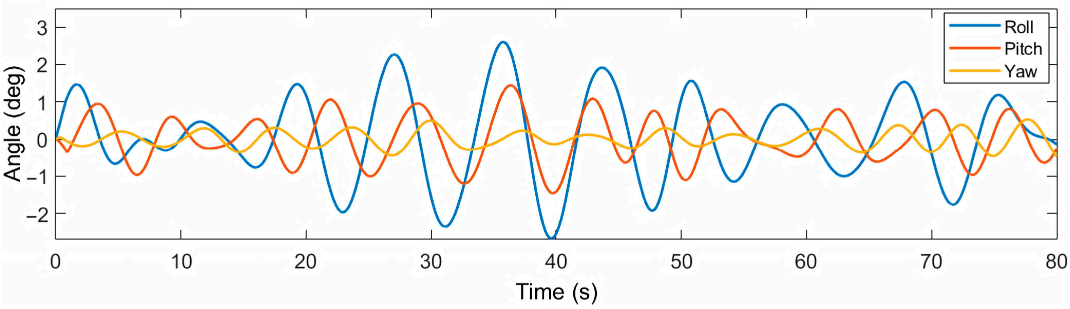

(**c**)

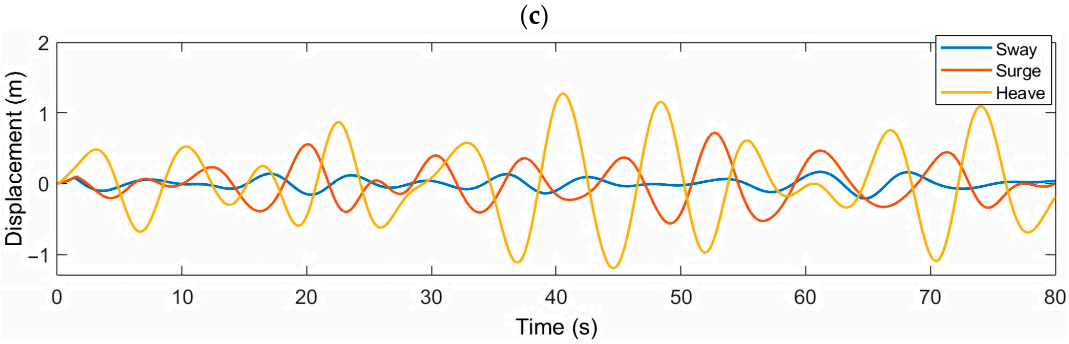

(**d**)

Figure 3. Six DOFs motion of the vessel. (**a**) The angle of roll, pitch, and yaw of the vessel when the encounter angle is 45 degrees. (**b**) The displacement of sway, surge, and heave of the vessel when the encounter angle is 45 degrees. (**c**) The angle of roll, pitch, and yaw of the vessel when the encounter angle is 90 degrees. (**d**) The displacement of sway, surge, and heave of the vessel when the encounter angle is 90 degrees.

4. Kinematic Model of the TAS

4.1. Forward Kinematics of the TAS

The setting of the coordinate system is shown in Figure 4. Point G is the center of the geodetic coordinate system, point V is the center of the ship's coordinate system, and point B is the geometric center of the base bottom of the TAS. In this study, G and V were set to coincide. In addition, V is the intersection of the ship's roll axis, pitch axis, and yaw axis. The installation position of the TAS is on the starboard side of the ship, parallel to and directly above the pitch axis, y_V. The distance between B and V on the y_V axis is B_y. The distance between B and V on the z_V axis is B_z.

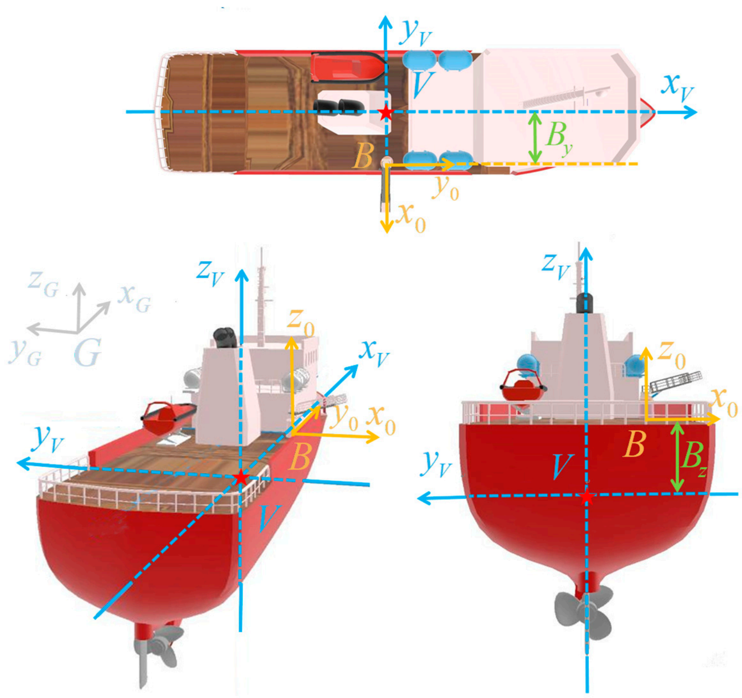

Figure 4. Coordinate system settings.

Therefore, the position of point B in the geodetic coordinate system {G} is:

$$
{}_{B}^{G}P = \begin{bmatrix} B_x \\ B_y \\ B_z \end{bmatrix} \tag{12}
$$

The motion modeling of the TAS focuses on the motion state of the end of the TAS device to obtain the motion state of the end effector under different sea conditions. This study employed Denavit–Hartenberg (D-H) parameters to determine the motion state based on the connecting rod parameters.

The coordinate system for the TAS is established in Figure 5. Coordinate system {0} is positioned at the geometric midpoint of the base bottom, while coordinate system {1} is located at the intersection of the rotary and pitch joints. Additionally, coordinate system {2} is established on the pitch arm. While the Y-axis shifts in tandem with the pitch arm movement, the coordinate origin remains identical to {1}. The coordinate system {3} is established at the intersection of the pitch and telescopic arms, and the z-axis points in the telescopic direction. The coordinate system {4} is established at the end of the telescopic arm, namely the end effector of the TAS. According to the D-H parameters, the four parameters between the two joints can be determined: connecting rod length, a_{i-1}, torsion angle, α_{i-1}, connecting rod offset, d_i, and joint angle, θ_i, as shown in Table 3.

In this study, the parameters, such as the rotary joint angle, α, pitch joint angle, β, and variable telescopic length, T, are limited according to the design requirements. L_1 is the distance in the Z-axis from the origin of the coordinate system {0} to the origin of coordinate system {1}. L_2 is the distance between the origin of the coordinate system {0} and the origin of the coordinate system {1} in the X-axis. L_3 is the length of the TAS when the telescopic joint is not used. L_5 is the width of the passageway of the TAS. L_6 is the diameter of the base.

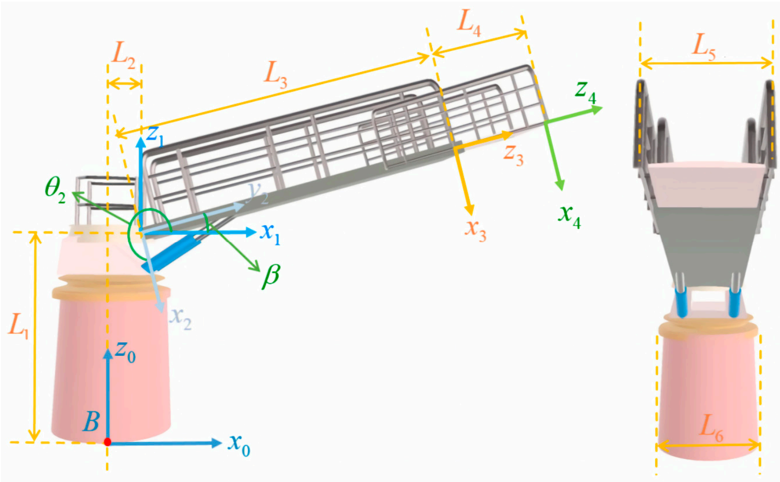

Figure 5. Coordinate system and D-H parameters of the TAS.

Table 3. D-H parameters.

i	a_{i-1}	α_{i-1}	d_i	θ_i
1	0	L_2	L_1	θ_1
2	$\pi/2$	0	0	θ_2
3	$-\pi/2$	0	L_3	0
4	0	0	L_4	0

The following equation can be obtained, as:

$$\begin{cases} \theta_1 = \alpha \\ \theta_2 = \frac{3}{2}\pi + \beta \\ L_4 = T \end{cases} \tag{13}$$

The coordinate transformation matrix of the latter coordinate system $\{i\}$ relative to the previous coordinate system $\{i-1\}$ can be obtained. It can be expressed as:

$${}^{i-1}_{i}T = \begin{bmatrix} {}^{i-1}_{i}R & {}^{i-1}P_{iORG} \\ 0 & 1 \end{bmatrix} = \begin{bmatrix} c\theta_i & -s\theta_i & 0 & a_{i-1} \\ s\theta_i c\alpha_{i-1} & c\theta_i c\alpha_{i-1} & -s\alpha_{i-1} & -s\alpha_{i-1}d_i \\ s\theta_i s\alpha_{i-1} & c\theta_i s\alpha_{i-1} & c\alpha_{i-1} & c\alpha_{i-1}d_i \\ 0 & 0 & 0 & 1 \end{bmatrix} \tag{14}$$

where ${}^{i-1}_{i}R$ is the rotation matrix of the coordinate system $\{i\}$ relative to the coordinate system $\{i-1\}$, and ${}^{i-1}P_{iORG}$ is the position vector of the origin of the coordinate system $\{i\}$ relative to the origin of the coordinate system $\{i-1\}$, $c\theta_i$ is the abbreviation of $\cos\theta_i$, $s\theta_i$ is the abbreviation of $\sin\theta_i$, and so on.

According to Table 3, the transformation matrix of the latter coordinate system relative to the previous coordinate system can be calculated as:

$${}^{0}_{1}T = \begin{bmatrix} \cos\theta_1 & -\sin\theta_1 & 0 & L_2 \\ \sin\theta_1 & \cos\theta_1 & 0 & 0 \\ 0 & 0 & 1 & L_1 \\ 0 & 0 & 0 & 1 \end{bmatrix} \tag{15}$$

$${}^{1}_{2}T = \begin{bmatrix} \cos\theta_2 & -\sin\theta_2 & 0 & 0 \\ 0 & 0 & -1 & 0 \\ \sin\theta_2 & \cos\theta_2 & 0 & 0 \\ 0 & 0 & 0 & 1 \end{bmatrix} \tag{16}$$

$$ {}_{3}^{2}T = \begin{bmatrix} 1 & 0 & 0 & 0 \\ 0 & 0 & 1 & L_3 \\ 0 & -1 & 0 & 0 \\ 0 & 0 & 0 & 1 \end{bmatrix} \tag{17} $$

$$ {}_{4}^{3}T = \begin{bmatrix} 1 & 0 & 0 & 0 \\ 0 & 1 & 0 & 0 \\ 0 & 0 & 1 & L_4 \\ 0 & 0 & 0 & 1 \end{bmatrix} \tag{18} $$

The transformation matrix of the end of the TAS relative to the base can be obtained as:

$$ {}_{4}^{0}T = {}_{1}^{0}T{}_{2}^{1}T{}_{3}^{2}T{}_{4}^{3}T = \begin{bmatrix} c\theta_1 c\theta_2 & -s\theta_1 & -c\theta_1 s\theta_2 & L_2 - (L_3 + L_4)c\theta_1 s\theta_2 \\ c\theta_2 s\theta_1 & c\theta_1 & -s\theta_1 s\theta_2 & -(L_3 + L_4)s\theta_1 s\theta_2 \\ s\theta_2 & 0 & c\theta_2 & L_1 + L_3 c\theta_2 + L_4 c\theta_2 \\ 0 & 0 & 0 & 1 \end{bmatrix} \tag{19} $$

The displacement of the TAS end effector relative to the base can be obtained from Equation (19) as:

$$ \begin{bmatrix} Tx \\ Ty \\ Tz \end{bmatrix} = \begin{bmatrix} L_2 - (L_3 + L_4)c\theta_1 s\theta_2 \\ -(L_3 + L_4)s\theta_1 s\theta_2 \\ L_1 + (L_3 + L_4)c\theta_2 \end{bmatrix} \tag{20} $$

In addition, since the base of the TAS and the center of the hull are not coincident, the coordinate transformation matrix of the base $\{B\}$ relative to the vessel center $\{V\}$ can be defined as:

$$ {}_{B}^{V}T = \begin{bmatrix} 0 & 1 & 0 & B_x \\ -1 & 0 & 0 & B_y \\ 0 & 0 & 1 & B_z \\ 0 & 0 & 0 & 1 \end{bmatrix} \tag{21} $$

where B_x, B_y, and B_z are the offsets of the base on the x-axis, y-axis, and z-axis relative to the hull center.

As the ship is always disturbed by wind, waves, and currents when sailing on the sea, the hull center moves with six degrees of freedom relative to the ground coordinate system [36]. In the research, the geodetic coordinate system $\{G\}$ was set at the position of the hydrodynamic coordinate system $\{H\}$. Equation (22) provides a description of the coordinate transformation matrix for the hull center concerning the ground coordinate system:

$$ {}_{V}^{G}T = \begin{bmatrix} c\psi c\theta & c\psi s\theta s\varphi - s\psi c\varphi & c\psi s\theta c\varphi + s\psi c\varphi & x \\ s\psi c\theta & s\psi s\theta s\varphi + c\psi c\varphi & s\psi s\theta c\varphi - c\psi s\varphi & y \\ -s\theta & c\theta s\varphi & c\theta c\varphi & z \\ 0 & 0 & 0 & 1 \end{bmatrix} \tag{22} $$

where φ is the roll angle, θ is the pitch angle, ψ is the yaw angle, x is the sway displacement, y is the surge displacement, and z is the heave displacement.

The transformation matrix of the TAS end effector relative to the ground coordinate system can be calculated as:

$$ {}_{4}^{G}T = {}_{V}^{G}T \cdot {}_{B}^{V}T \cdot {}_{4}^{0}T \tag{23} $$

Finally, according to Equation (23) and Table 4, the reachable working space of the TAS within the specified rotation joint angle, pitch joint angle, and telescopic length limits can be obtained, as shown in Figure 6.

Table 4. Motion parameters of the TAS.

Parameter	Value
α	$-20°$~$20°$
β	$-20°$~$20°$
L_1	2.32 m
L_2	0.325 m
L_3	3.625 m
L_4	0~1.2 m
L_5	0.9 m
L_6	1.47 m

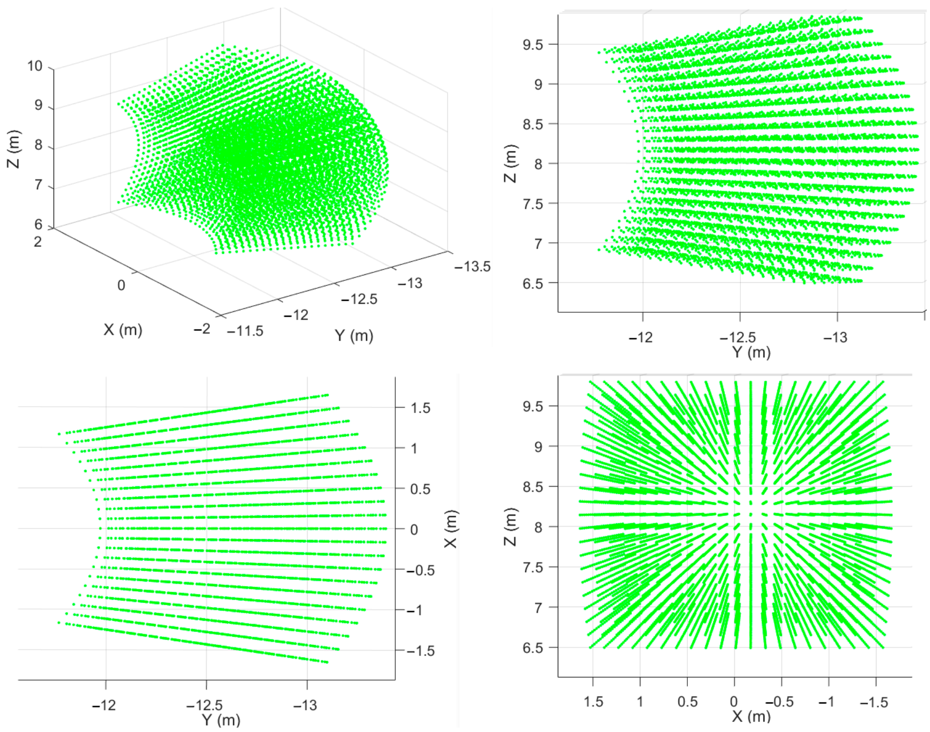

Figure 6. Reachable working space of the TAS.

It is easy to see that the TAS in this study has a wide workspace and the outermost side of the workspace is curved. The workspace ranges −1.65 m~1.65 m on the *x*-axis, −13.38 m~−11.77 m on the *y*-axis, and 6.49 m~9.79 m on the *z*-axis. The maximum distance of the TAS in the workspace on the *x*-axis is greater than its telescopic length, L_4, which is due to the curved surface formed at the edge of the workspace at the end of the TAS, and the distance between the edges of the two curved surfaces is greater than the width of the inner side, as can be seen from the first image in Figure 6.

4.2. Compensation Value

A superimposed compensation scheme is proposed to obtain appropriate compensation values. By analyzing the effects of pitch, roll, and heave on the end of the TAS separately, appropriate rotary joint angles, pitch joint angles, and telescopic lengths were determined. Finally, the sum of the three obtained rotation rotary joint angles, pitch joint angles, and telescopic lengths is the target compensation value.

In order to reduce the difficulty of solving and simplify the solving process, the simplified TAS model was used here to replace the TAS model in Figure 7.

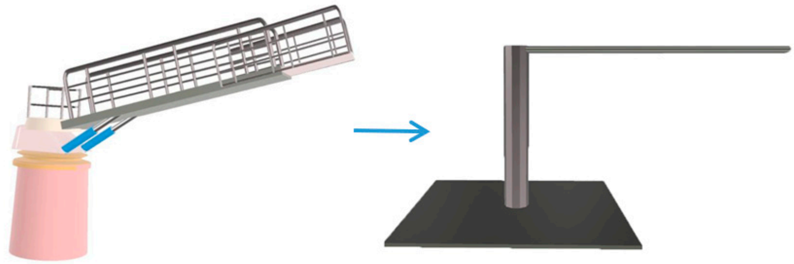

Figure 7. Model simplification.

As shown in Figure 7, the simplified model combines the base and rotary joint of the pre-simplified model into a standing cylinder. In addition, the simplified model integrates the arm of the pitch joint and the telescopic joint.

4.2.1. Pitch Compensation

In Figure 8, the position of the TAS when not affected by waves is shown in black. When the pitch angle is θ, the TAS moves to the position shown in gold in the figure. Among them, p is the position at the end of the TAS when there are no waves, and it is also the position that the end of the TAS needs to be compensated for. p_2 is the center of the {1} coordinate system of the TAS when the pitch angle is θ, p_6 is the center of the top of the column where the rotary joint is located, p_4 is the position of the end of the bridge device when the pitch angle is θ, p_3 represents the position of the TAS after rotation α_1 for compensation, which is the rotary joint angle, and p_1 represents the position of the TAS after rotation β_1 for compensation, which is the pitch joint angle.

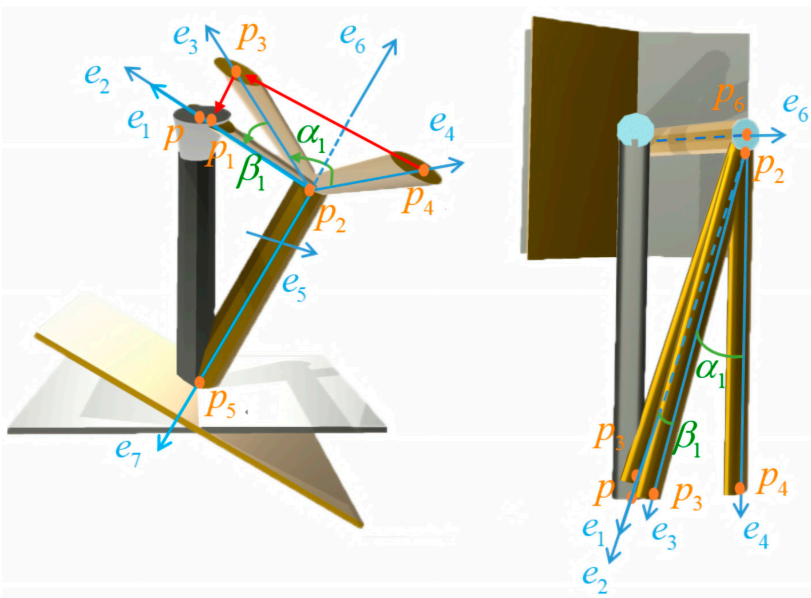

Figure 8. Pitch compensation.

The compensation process is shown by the red arrow. At the end of the bridge-crossing device, the rotation angle of the rotary joint is adjusted from position p_4 to p_3, then the rotation angle of the pitch joint is adjusted from p_3 to p_1. Finally, the expansion joint is adjusted to extend the end to p_1, and the telescopic length is T_1. Therefore, α_1, β_1, and T_1 need to be solved.

The required rotation joint angle and pitch joint angle require the position of p_3 or the direction of vector e_3. It can be seen that the straight line p_2p_3 is on plane $p_3p_4p_2$ and on plane $p_1p_2p_5$, which means that the straight line p_2p_3 is the intersection of two planes. To obtain the direction of p_2p_3, the normal vectors of these two planes are simply obtained, which are e_5 and e_6.

The coordinates of points p, p_2, p_4, and p_5 can all be calculated using Equation (23).

In order to achieve complete compensation, it is necessary to point the TAS end p_1 that has undergone rotation joint compensation and pitch joint compensation towards the target point p, where points p, p_1, and p_2 are in a straight line. The vector e_1 pointing from point p_2 to p_1 and the vector e_2 pointing from point p_2 to p are in the same direction; then, vector e_2 is:

$$e_2 = \begin{bmatrix} p_x - p_{2x} \\ p_y - p_{2y} \\ p_z - p_{2z} \end{bmatrix} \tag{24}$$

where p_x is the abscissa of point p, p_{2y} is the ordinate of point p_2, and so on.

Since e_1 and e_2 are in the same direction and the initial TAS arm length is L, the coordinates of point p_1 are:

$$\begin{cases} p_1 = p_2 + \frac{e_2}{|e_2|} \cdot L \\ L = L_3 + d_0 \end{cases} \tag{25}$$

where L_3 is the length of the pitch joint, which can be obtained from Table 4, and d_0 is the length of the telescopic joint and was set to 0.5 in this study.

The vector e_7 pointing from point p_2 to p_5 is:

$$e_7 = \begin{bmatrix} p_{5x} - p_{2x} \\ p_{5y} - p_{2y} \\ p_{5z} - p_{2z} \end{bmatrix} \tag{26}$$

The vector e_5 is the cross-product of e_1 and e_7, and e_5 is also the normal vector of the surface $p_3p_2p_5$, which can be determined by the following equation:

$$e_5 = e_1 \times e_7 \tag{27}$$

The direction of the normal vector e_6 of plane $p_3p_2p_4$ is:

$$e_6 = \begin{bmatrix} p_{5x} - p_{6x} \\ 0 \\ p_{5z} - p_{6z} \end{bmatrix} \tag{28}$$

The vector e_3 is the intersection of plane $p_3p_2p_5$ and plane $p_3p_2p_4$, which can be determined by the following equation:

$$e_3 = e_5 \times e_6 \tag{29}$$

The rotation joint angle α_1 is the angle between vectors e_3 and e_4, and it can be calculated as:

$$\alpha_1 = \arccos\left(\frac{e_3 \cdot e_4}{|e_3||e_4|}\right) \tag{30}$$

The pitch joint angle β_1 is the angle between vectors e_3 and e_2, and it can be calculated as:

$$\beta_1 = \arccos\left(\frac{e_3 \cdot e_2}{|e_3||e_2|}\right) \tag{31}$$

The telescopic length T_1 is the distance between points p and p_1, and it can be calculated as:

$$T_1 = \sqrt{(p_x - p_{1x})^2 + (p_y - p_{1y})^2 + (p_y - p_{1y})^2} \tag{32}$$

In addition, the α_1, β_1, and T_1 calculated above are only numerical values, and different directions need to be added for correct compensation for different movements.

When the pitch angle θ is negative (the ship tilts forward), the swing arm of the TAS should move to the right and extend forward:

$$\begin{cases} \alpha_1 = -\alpha_1 \\ \beta_1 = -\beta_1 \\ T_1 = T_1 \end{cases} \tag{33}$$

When the pitch angle is positive (the ship tilts backwards), the swing arm of the bridge-crossing device should move to the left and extend forward:

$$\begin{cases} \alpha_1 = \alpha_1 \\ \beta_1 = \beta_1 \\ T_1 = T_1 \end{cases} \tag{34}$$

4.2.2. Roll Compensation

In Figure 9, the TAS when not affected by waves is shown in black. When the roll angle is φ, the TAS moves to the position shown in gold in the figure. p_9 is the position of the TAS end when there are no waves, and it is also the target position of the TAS end. p_{10} is the center of the {1} coordinate system of TAS when the roll angle is φ. p_7 is the position of the TAS end when the roll angle is φ. p_8 represents the position of the TAS after rotating β_2 for compensation; that is, β_2 represents the pitch joint angle. It is worth mentioning that there is no need to use the rotary joint angle in roll compensation, as the TAS only performs longitudinal motion under the influence of roll, so rotary joint angle α_2 = 0.

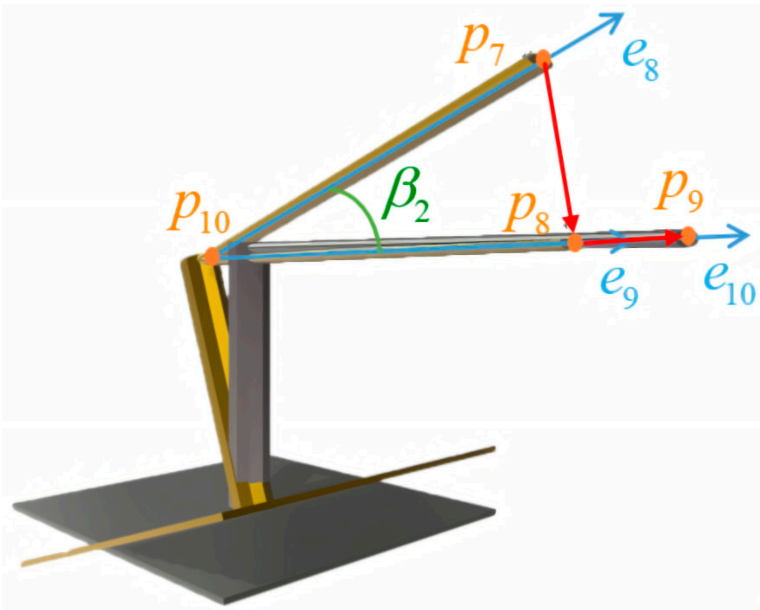

Figure 9. Roll compensation.

The compensation process is indicated by the red arrow. The pitch joint is rotated β_2 degrees to move the end from position p_7 to p_8, and then the extension joint is extended T_2 to p_9. Therefore, β_2 and p_9 need to be solved.

The coordinates of points p_7, p_9, and p_{10} can all be calculated using Equation (23).

The vector e_8 pointing from point p_{10} to p_7 is:

$$e_8 = \begin{bmatrix} p_{7x} - p_{10x} \\ p_{7y} - p_{10y} \\ p_{7z} - p_{10z} \end{bmatrix} \tag{35}$$

To achieve complete compensation, it is necessary to point the vector e_9 from point p_{10} to p_8 and to the target position p_{10}. The vector e_{10} pointing from p_{10} to p_9 is in the same direction as e_9. e_{10} can be calculated as:

$$e_{10} = \begin{bmatrix} p_{9x} - p_{10x} \\ p_{9y} - p_{10y} \\ p_{9z} - p_{10z} \end{bmatrix} \tag{36}$$

The pitch joint angle β_2 is the angle between vectors e_8 and e_{10}:

$$\beta_2 = \arccos\left(\frac{e_8 \cdot e_{10}}{|e_8||e_{10}|}\right) \tag{37}$$

Since e_9 and e_{10} are in the same direction and the initial TAS arm length is L, the coordinates of point p_8 are:

$$\begin{cases} p_8 = p_{10} + \frac{e_{10}}{|e_{10}|} \cdot L \\ L = L_3 + d_0 \end{cases} \tag{38}$$

The elongation T_2 that needs to be adjusted for the telescopic joint is the distance between points p_8 and p_9:

$$T_2 = \sqrt{(p_{8x} - p_{9x})^2 + (p_{8y} - p_{9y})^2 + (p_{8y} - p_{9y})^2} \tag{39}$$

In addition, the α_2, β_2, and T_2 calculated above are only numerical values, and different directions need to be added for correct compensation for different movements.

When the roll angle φ is negative (the ship tilts left), the swing arm of the TAS should move downward and extend forward:

$$\begin{cases} \alpha_2 = 0 \\ \beta_2 = -\beta_2 \\ T_2 = T_2 \end{cases} \tag{40}$$

When the roll angle φ is positive (the ship tilts to the right), the swing arm of the TAS should move upwards and shorten backwards:

$$\begin{cases} \alpha_2 = 0 \\ \beta_2 = \beta_2 \\ T_2 = -T_2 \end{cases} \tag{41}$$

4.2.3. Heave Compensation

In Figure 10, the TAS when not affected by waves is shown in black. When the heave height is z, the TAS moves to the position shown in gold. p_{11} is the center of the {1} coordinate system of TAS when the heave height is z. p_{12} is the position of the TAS end when the heave height is z. p_{14} is the center of the {1} coordinate system of the TAS when there are no waves. p_{15} compensates for the position of the TAS after rotating by β_3 degrees; that is, β_3 is the pitch joint angle. p_{16} is the position of the TAS end when there are no waves, and it is also the target position of the TAS. Cross-pointing p_{15} creates a perpendicular intersection line segment $p_{13}p_{14}$, with the intersection point at point p_{13}. Cross-pointing p_{15} makes a perpendicular line that intersects line segment $p_{14}p_{16}$, with the intersection point being point p_{17}. It is worth mentioning that, similar to roll compensation, there is no need to retrieve the rotary joint angle α_3 in heave compensation, as the TAS only moves in the vertical plane under the influence of heave, so α_3 = 0.

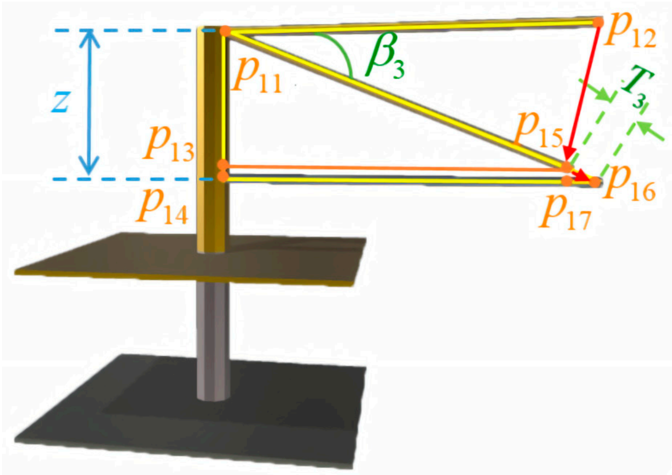

Figure 10. Heave compensation.

The compensation process is indicated by the red arrow. The pitch joint is rotated β_3 degrees to move the end from p_{12} to p_{15}, and then the telescopic joint is extended T_3 to p_{16}. Therefore, T_3 needs to be solved.

Since $p_{11}p_{12} \parallel p_{14}p_{16}$, the pitch joint angle β_3 can be calculated as:

$$\begin{cases} \angle\beta_3 = \angle p_{11}p_{16}p_{14} = \arctan(\frac{z}{L}) \\ L = L_3 + d_0 \end{cases} \tag{42}$$

As the three angles of $\triangle p_{11}p_{14}p_{16}$ and $\triangle p_{15}p_{17}p_{16}$ are completely equal, and it can be concluded that $\triangle p_{11}p_{14}p_{16} \sim \triangle p_{15}p_{17}p_{16}$, the proportion relationship of edges can be represented as:

$$\frac{p_{11}p_{13}}{p_{11}p_{15}} = \frac{p_{15}p_{17}}{p_{15}p_{16}} \tag{43}$$

Equation (43) can be represented as:

$$\frac{L\sin\beta_3}{L} = \frac{|z| - L\sin\beta_3}{T_3} \tag{44}$$

where $|z|$ is the absolute value of the heave height z.

Solving Equation (44), the telescopic length T_3 can be calculated as:

$$T_3 = \frac{|z|}{\sin\beta_3} - L \tag{45}$$

In addition, α_3, β_3, and T_3 are only numerical values, and different directions need to be added for correct compensation for different movements.

When z is positive (when the ship rises), the swing arm of the TAS should move downward and extend forward:

$$\begin{cases} \alpha_3 = 0 \\ \beta_3 = -\beta_3 \\ T_3 = T_3 \end{cases} \tag{46}$$

When z is negative (ship descending), the swing arm of the TAS should move upwards and extend forward:

$$\begin{cases} \alpha_3 = 0 \\ \beta_3 = \beta_3 \\ T_3 = T_3 \end{cases} \tag{47}$$

Finally, by adding the rotation joint angle, pitch joint angle, and telescopic joint angle from the three compensations above, the obtained sum is the final rotary joint angle α, pitch joint angle β, and telescopic joint length T, which can be represented as:

$$\begin{cases} \alpha = \alpha_1 + \alpha_2 + \alpha_3 \\ \beta = \beta_1 + \beta_2 + \beta_3 \\ T = T_1 + T_2 + T_3 \end{cases} \tag{48}$$

The values of α, β, and T are limited by Table 4.

In addition, according to the results obtained in this study, ship pitch compensation requires the participation of the rotary joint, pitch joint, and expansion joint in the compensation. The roll compensation and heave compensation of ships require the participation of pitch and expansion joints. That is, the rotary joint determines the pitch compensation ability, while the pitch joint and expansion joint determine the roll, pitch, and heave compensation results of the ship. If the rotation angle and pitch angle range of the TAS's rotation joint are larger, and the expansion joint and extension length are longer, then the TAS's workspace will be larger, and it can cope with more severe sea conditions.

5. Hydraulic Servo System Modeling of TAS

The hydraulic cylinder can be classified into two types, namely the symmetrical cylinder and the asymmetrical cylinder, based on the area being the same on both sides of the piston. The asymmetrical cylinder has an edge over the symmetrical cylinder since it does not comprise a piston rod component at the other end, thereby reducing the cylinder volume and occupying less space. In this study, among the three joints of the TAS, except the rotary joint, which uses a four-way valve symmetrical cylinder, the pitch joint and the telescopic joint both use a four-way valve asymmetrical cylinder.

5.1. Four-Way Valve-Controlled Symmetrical Cylinder

5.1.1. Flow Equation of Slide Valve

The structure of the four-way valve-controlled symmetrical cylinder is shown in Figure 11. The piston of a symmetrical hydraulic cylinder has the same diameter in both directions of motion, resulting in an equal effective area on both sides. This makes the driving force and speed of the hydraulic cylinder similar in both directions. Q_1 is the total amount of hydraulic oil flowing into the valve-controlled hydraulic cylinder, and Q_2 is the total amount of hydraulic oil flowing out of the valve-controlled hydraulic cylinder.

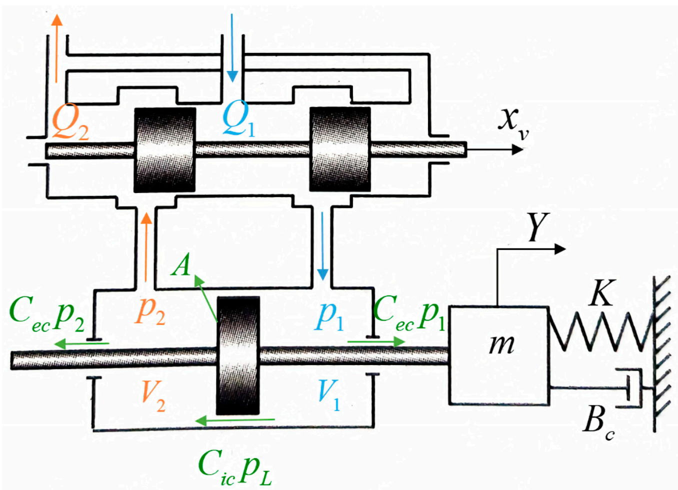

Figure 11. Structure of the four-way valve-controlled symmetrical cylinder.

For the change in oil quantity entering the valve-controlled symmetrical cylinder, ΔQ_1, and the change in oil quantity exiting the valve-controlled symmetrical cylinder, ΔQ_2, the following equations are established:

$$\Delta Q_1 = K_q \Delta x_v - 2K_c \Delta p_1 \tag{49}$$

$$\Delta Q_2 = K_q \Delta x_v + 2K_c \Delta p_2 \tag{50}$$

where K_q is the flow gain, K_c is the pressure–flow coefficient, p_1 is the left chamber pressure, p_2 is the right chamber pressure, and x_v is displacement of the spool valve.

Adding Equations (51) and (52), the change of load flow, ΔQ_L, can be expressed as:

$$\Delta Q_L = \frac{\Delta Q_1 + \Delta Q_2}{2} = K_q \Delta x_v - K_c \Delta p_L \tag{51}$$

$$p_L = p_1 - p_2 \tag{52}$$

where p_L is the load pressure drop.

Due to the piston moving slightly near the stable working point most of the time, the load flow, Q_L, can be expressed as:

$$Q_L = K_q x_v - K_c p_L \tag{53}$$

5.1.2. Flow Equation of Hydraulic Cylinder

For the flow into the hydraulic cylinder, Q_{in}, and the flow out of the hydraulic cylinder, Q_{out}, the continuous equation of compressed fluid can be expressed as:

$$Q_{\text{in}} - Q_{out} = \frac{\mathrm{d}V}{dt} + \frac{V}{\beta} \cdot \frac{dp}{dt} \tag{54}$$

$$V_t = V_1 + V_2 = 2V_0 \tag{55}$$

$$Q_{in} = Q_1 - C_{ic}(p_1 - p_2) - C_{ec} p_1 = A\frac{dY}{dt} + \frac{V_0}{\beta_e} \cdot \frac{dp_1}{dt} \tag{56}$$

$$Q_{out} = C_{ic}(p_1 - p_2) - C_{ec} p_1 - Q_2 = -A\frac{dY}{dt} + \frac{V_0}{\beta_e} \cdot \frac{dp_2}{dt} \tag{57}$$

$$Q_L = \frac{Q_1 + Q_2}{2} \tag{58}$$

where V is the initial volume of the chamber liquid, Δp is the change in chamber pressure, β_e is the equivalent bulk modulus, V_t is the total volume of the hydraulic cylinder, V_1 and V_2 are the volumes of two hydraulic chambers, respectively, V_0 is the volume of each side when the piston is in the middle of the chamber, A is the effective area of the piston, and Y is the displacement of the hydraulic cylinder piston.

Substituting Equations (55)–(58) into Equation (54), the flow equation of the hydraulic cylinder can be obtained:

$$Q_L = A\frac{dY}{dt} + C_{tc} p_L + \frac{V_t}{4\beta_e} \cdot \frac{dp_L}{dt} \tag{59}$$

where $C_{tc} = C_{\text{ic}} + \frac{1}{2} C_{ec}$ is the total leakage coefficient, C_{ic} is the internal leakage coefficient, and C_{ec} is the external leakage coefficient.

5.1.3. Flow Equation of Slide Valve

According to Newton's second law, we can obtain:

$$F_g = A p_{_L} = m\frac{d^2Y}{dt^2} + B_c \frac{dY}{dt} + KY + F \tag{60}$$

where m is the total mass of piston and load, Y is the displacement of the hydraulic rod, B_c is the viscous damping coefficient of piston and load, K is the spring stiffness of load, F is the external force applied on the piston, and F_g is the hydraulic driving force.

According to Equations (53), (59), and (60), ignoring the spring stiffness of load K, the transfer function between the piston displacement Y and slide valve displacement x_v of a symmetric hydraulic cylinder can be calculated as:

$$\frac{Y}{x_v} = \frac{\frac{K_q}{A}}{s\left(\frac{s^2}{\omega_h^2} + \frac{2\zeta_h}{\omega_h}s + 1\right)} \tag{61}$$

$$\omega_h = \sqrt{\frac{4\beta_e A^2}{V_t m}} \tag{62}$$

$$\zeta_h = \frac{K_{ce}}{A}\sqrt{\frac{B_c m}{V_t}} \tag{63}$$

$$K_{ce} = K_c + C_{ic} + \frac{C_{ce}}{2} \tag{64}$$

where ω_h is the hydraulic natural frequency, ζ_h is the hydraulic damping ratio, and K_{ce} is the total flow–pressure coefficient.

The relevant parameters of the rotary joint are listed in Table 5.

Table 5. The relevant parameters of the rotary joint.

Parameter	Value
K_q	$5.560 \times 10^{-5}\ \mathrm{m^3/(s \cdot V)}$
K_{ce}	$1.8 \times 10^{-11}\ \mathrm{m^3/(s \cdot Pa)}$
A	$0.001\ \mathrm{m^3}$
β_e	$6.9 \times 10^{8}\ \mathrm{N/m^2}$
V_t	$8.762 \times 10^{-4}\ \mathrm{m^3}$
m	1600 kg
B_c	$5000\ \mathrm{N/(m/s)}$

According to Table 5, the transfer function of a symmetric hydraulic cylinder can be calculated as:

$$Y_{rotray}(s) = \frac{0.056}{s\left(\frac{s^2}{44.662^2} + \frac{2\times 0.676s}{44.662} + 1\right)} \tag{65}$$

5.2. Four-Way Valve-Controlled Asymmetric Cylinder

The difference from the symmetrical cylinder of the four-way slide valve is that the effective area of the piston is different during extension and retraction. The structure of the asymmetric valve-controlled hydraulic cylinder is shown in Figure 12. This design can be used to generate motion with different speeds and forces. This is suitable for the pitch joint and the telescope joint, as the pitch joint requires greater force when lifted and the telescope joint when extended, while the opposite movement can achieve faster speed. In addition, p_s is the fuel supply pressure, and p_0 is the return pressure.

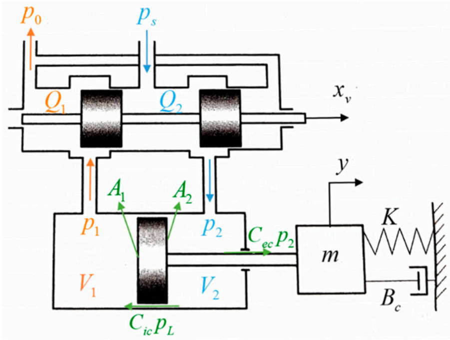

Figure 12. Structure of the asymmetric valve-controlled hydraulic cylinder.

5.2.1. Flow Equation of Slide Valve

The effective area ratio of the left and right cavities of the hydraulic cylinder can be set as $n = \frac{A_2}{A_1}$. The flow equation of the slide valve can be defined as:

$$Q_L = K_q x_v - K_c p_L \tag{66}$$

$$K_q = \begin{cases} K_{q1} = C_d W \sqrt{\frac{2}{\rho}\left(\frac{p_s - p_L}{1+n^3}\right)}, x_v > 0 \\ K_{q2} = C_d W \sqrt{\frac{2}{\rho}\left(\frac{np_s + p_L}{1+n^3}\right)}, x_v < 0 \end{cases} \tag{67}$$

$$K_c = \begin{cases} K_{c1} = C_d W x_v \sqrt{\frac{1}{2\rho(p_s - p_L)(1+n^3)}}, x_v > 0 \\ K_{c2} = -C_d W x_v \sqrt{\frac{1}{2\rho(np_s + p_L)(1+n^3)}}, x_v < 0 \end{cases} \tag{68}$$

$$p_L = p_1 - np_2 \tag{69}$$

$$Q_L = \frac{Q_1 + nQ_2}{1+n^2} \tag{70}$$

where C_d is the flow coefficient of the throttling port, generally taken as 0.60~0.65, W is the area gradient, ρ is the density of liquid, p_s is the fuel supply pressure, p_L is the load pressure drop, x_v is the spool displacement of the slide valve, K_{q1} and K_{q2} are the flow gains when $x_v > 0$ and $x_v < 0$, respectively, while K_{c1} and K_{c2} are the pressure–flow gains when $x_v > 0$ and $x_v < 0$, respectively.

5.2.2. Flow Equation of Hydraulic Cylinder

Assuming that the initial volumes of the two chambers of the piston are equal, the following equations can be obtained:

$$V_{10} = V_{20} = \frac{V_t}{2} \tag{71}$$

$$A_1 x_p \ll \frac{V_t}{2} \tag{72}$$

$$A_2 x_p \ll \frac{V_t}{2} \tag{73}$$

where V_{10} and V_{20} are the initial volumes of the two chambers of the hydraulic cylinder, and V_t is the total volume of the two chambers.

According to Equations (70), (72), and (73), the flow equation of the hydraulic cylinder can be obtained as:

$$Q_L = A_p \frac{dy}{dt} + \frac{V_t}{2(1+n^2)\beta_e}\frac{dp_L}{dt} + C_t p_L + C_{tc} p_s \tag{74}$$

where β_e is the equivalent bulk modulus, C_t is the total leakage coefficient related to the pressure load, which can be obtained from Equation (75), and C_{tc} is the leakage coefficient related to the fuel supply pressure, which can be obtained from Equation (76):

$$C_t = \frac{n^2(n^2-1)}{(1+n^2)(1+n^3)} C_{ic} \tag{75}$$

$$C_{tc} = \begin{cases} C_{tc1} = \frac{1+n}{1+n^3} C_i + \frac{C_{ec}}{1+n^2}, x_v > 0 \\ C_{tc2} = \frac{n^2-1}{(1+n^3)(1+n^2)} C_{ic}, x_v < 0 \end{cases} \tag{76}$$

where C_{ic} and C_{ec} are the internal leakage coefficient and external leakage coefficient, respectively.

5.2.3. Force Balance Equation

The balance equation of the asymmetrical cylinder force of the four-way slide valve can be described as:

$$A_1 p_L = m\frac{d^2y}{dt^2} + B_c\frac{dy}{dt} + Ky + F \tag{77}$$

where m is the total mass of the piston and load, y is the displacement of the hydraulic rod, B_c is the viscous damping coefficient of the piston and load, and F is the external force applied on the piston.

Equations (66), (74), and (77) can be transformed by Laplace transform when the spring stiffness, K, of the load can be ignored. The transfer function between the displacement of the hydraulic rod, y, and the displacement of the valve core, x_v, can be expressed as:

$$\frac{y}{x_v} = \frac{\frac{K_q}{A_1}}{s\left(\frac{s^2}{\omega_h^2} + \frac{2\zeta_h}{\omega_h}s + 1\right)} \tag{78}$$

where ω_h is the hydraulic natural frequency, which can be obtained from Equation (79), and ζ_h is the hydraulic damping ratio, which can be obtained from Equation (80):

$$\omega_h = \sqrt{\frac{2(1+n^2)\beta_e A_1^2}{mV_t}} \tag{79}$$

$$\zeta_h = \frac{K_{ce}}{2A_1}\sqrt{\frac{2(1+n^2)\beta_e m}{V_t}} \tag{80}$$

where $K_{ce} = K_c + C_t$ is the total pressure–flow coefficient. Due to the completely different values of K_q and K_{ce} at $x_v > 0$ and $x_v < 0$, the molecular and hydraulic damping coefficients of the transfer function are also different.

The relevant parameters of the pitch joint are listed in Table 6.

Table 6. The relevant parameters of the pitch joint.

Parameter	Value
A_1	3.1×10^{-3} m^2
A_2	1.5×10^{-3} m^2
n	0.490
K_{q1}	2.333×10^{-3} m^3/(s · V)
K_{q2}	2.917×10^{-5} m^3/(s · V)
K_{ce1}	5.8×10^{-11} m^3/(s · Pa)
K_{ce2}	1.8×10^{-11} m^3/(s · Pa)
β_e	6.9×10^8 N/m^2
V_t	2.5×10^{-3} m^3
m	1150 kg
B_c	5000 N/(m/s)

According to Table 6, the transfer function of a symmetric hydraulic cylinder can be calculated as:

$$Y_{pitch}(s) = \begin{cases} \frac{0.0749}{s\left(\frac{s^2}{76.642^2} + \frac{2\times0.263s}{76.642} + 1\right)}, x_v > 0 \\ \frac{0.0936}{s\left(\frac{s^2}{76.642^2} + \frac{2\times0.816s}{76.642} + 1\right)}, x_v < 0 \end{cases} \tag{81}$$

The relevant parameters of the telescopic joint are listed in Table 7.

Table 7. The relevant parameters of the telescopic joint.

Parameter	Value
A_1	2.0×10^{-3} m^2
A_2	9.456×10^{-4} m^2
n	0.482
K_{q1}	1.111×10^{-3} m$^3/(\mathrm{s} \cdot \mathrm{V})$
K_{q2}	1.389×10^{-5} m$^3/(\mathrm{s} \cdot \mathrm{V})$
K_{ce1}	5.8×10^{-11} m$^3/(\mathrm{s} \cdot \mathrm{Pa})$
K_{ce2}	1.8×10^{-11} m$^3/(\mathrm{s} \cdot \mathrm{Pa})$
β_e	6.9×10^8 N/m^2
V_t	4.5×10^{-3} m^3
m	950 kg
B_c	5000 N/(m/s)

The transfer function of a symmetric hydraulic cylinder can be calculated as:

$$Y_{\text{telescopic}}(s) = \begin{cases} \frac{0.0566}{s\left(\frac{s^2}{39.116^2} + \frac{2\times0.280s}{39.116} + 1\right)}, x_v > 0 \\ \frac{0.0707}{s\left(\frac{s^2}{39.116^2} + \frac{2\times0.867s}{39.116} + 1\right)}, x_v < 0 \end{cases} \tag{82}$$

5.3. Model of Servo Valve

Since the natural frequency of the transfer function of the actuator is generally far lower than the frequency of the servo valve, the transfer function of the servo valve is generally regarded as a second-order unit or a first-order unit. It is mainly divided into the following three situations:

- If the response frequency of the servo valve is close to the natural frequency of the hydraulic cylinder, the servo valve can be regarded as a second-order oscillation unit.
- If the response frequency of the servo valve is 3~5 times that of the natural frequency of the hydraulic cylinder, the servo valve can be regarded as an inertial unit.
- If the response frequency of the servo valve is more than 5 times that of the natural frequency of the hydraulic cylinder, the servo valve can be regarded as a proportional unit.

In this study, the transfer function of the servo valve can be defined as:

$$g(s) = \frac{1}{0.035s + 1} \tag{83}$$

Due to the response frequency of the servo valve used in this study being 3–5 times the natural frequency, it is considered as an inertial unit, where 0.035 is the inertia constant of the servo valve.

6. Design of Controller

6.1. Fuzzy PID Controller

The PID controller has a simple structure and strong robustness. However, the parameters of ordinary PID cannot change with the sea state because the sea state changes rapidly. Therefore, fuzzy PID control was adopted here. The three parameters of fuzzy PID are not fixed but are provided in real time according to the external environment to ensure the real-time update of the PID control system. The schematic diagram of fuzzy PID is shown in Figure 13. The accurate input value is fuzzed by the membership function, then the fuzzed results are matched with the established fuzzy rules one-by-one, and finally, the matching result is anti-fuzzed to output the accurate value. The output results are transmitted to the PID controller, which controls the controlled object in real time.

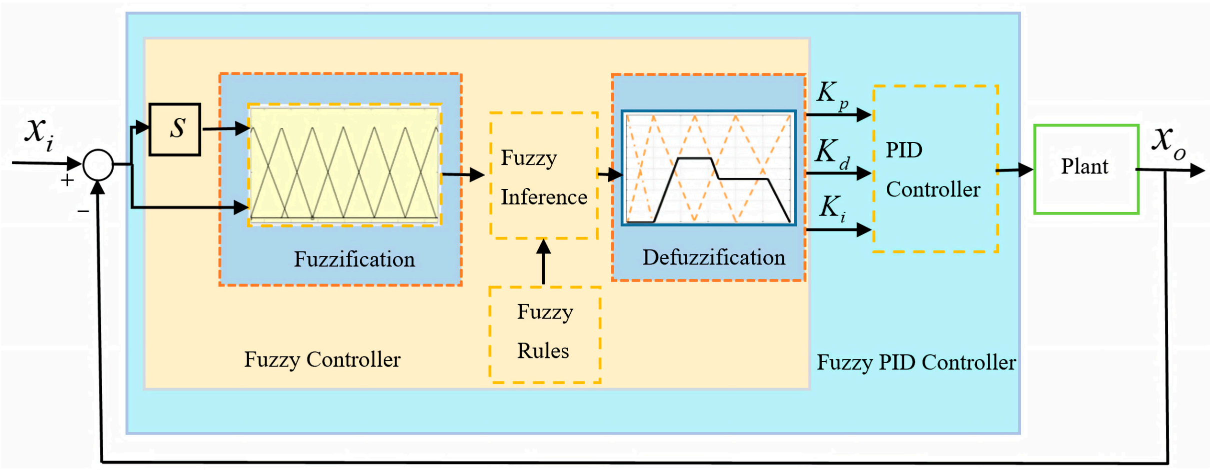

Figure 13. Schematic diagram of fuzzy PID.

In fuzzy PID control, the design of the fuzzy controller plays a vital role, determining whether the PID control is effective. The fuzzy control design of this study was as follows. First, input and output fuzzy subsets were defined, where {NB, NM, NS, ZO, PS, PM, PB} were defined as the input and output fuzzy subsets, representing Negative Big, Negative Medium, Negative Small, Zero, Positive Small, Positive Medium, and Positive Big, respectively.

The error e and the first derivative of the error ec were used as fuzzy input values. The value e range was (−0.035, 0.035), and the value ec range was (−0.5, 0.5). The range of K_p, K_i, and K_d was (0, 1). Then, the appropriate proportion coefficients were selected as the system parameters. Finally, the membership function and fuzzy rules were designed according to the experience of experts.

Moreover, the Mamdani algorithm was used for fuzzy inference, and the centroid algorithm was used for defuzzification. The fuzzy regular surfaces obtained from the above parameters are shown in Figure 14.

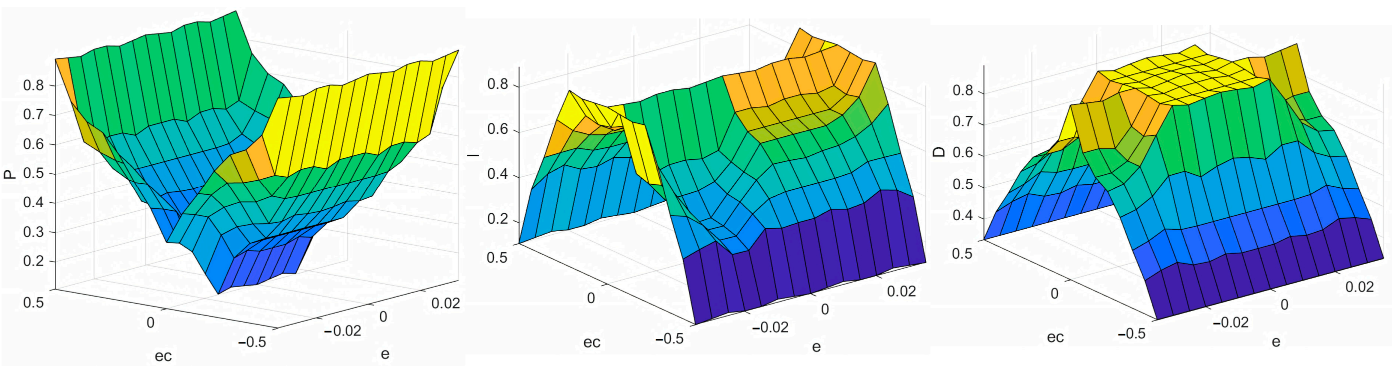

Figure 14. Fuzzy regular surfaces of P, I, and D in fuzzy control. Different colors represent different values, and the larger the value, the warmer the color tone.

From Figure 14, it can be observed that when there is a significant error between the input and output, K_p is increased to achieve rapid error reduction, thereby improving the dynamic performance of the system and reducing K_i and K_d to prevent system instability.

When the error between the input and output is small, K_p should be reduced to prevent excessive overshoot, while K_i and K_d should be increased to improve speed.

6.2. Feedforward Compensation

In order to improve the stability and speed of the system and reduce errors, feedforward compensation was added in three joints. Figure 15 shows the composition structure of the hydraulic control system using the rotary joint as an example. K_f is the transfer function of the angle sensor, $G_p(s)$ is the transfer function of the fuzzy PID controller, K_a is the transfer function of the power amplification unit, $G_v(s)$ is the transfer function of the servo valve, $G_c(s)$ is the transfer function of the hydraulic cylinder, and $G_r(s)$ is the feedforward compensation unit that needs to be designed.

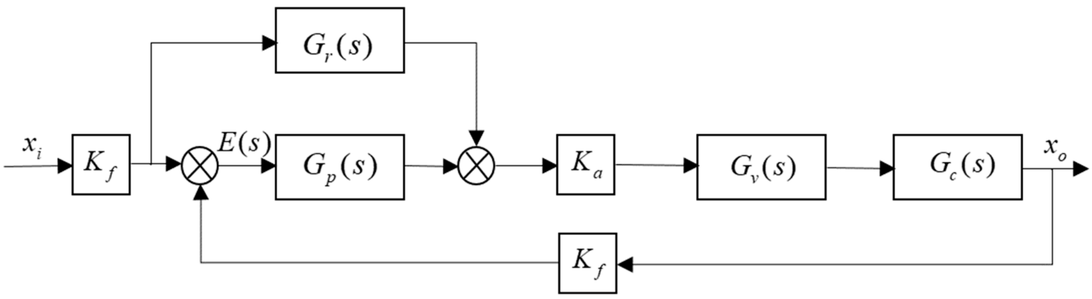

Figure 15. Feedforward compensation of the rotary joint.

The output x_o of the system is obtained from the following equation:

$$x_o = K_a G_v(s) G_c(s) \Big(E(s) G_p(s) + K_f G_r(s) x_i \Big) \tag{84}$$

where $E(s)$ can be obtained by the following equation:

$$E(s) = K_f(x_i - x_o) \tag{85}$$

It can be inferred that:

$$\frac{x_o}{x_i} = \frac{K_f\big(G_r(s) + G_p(s)\big)}{\frac{1}{K_a G_v(s) G_c(s)} + K_f G_p(s)} \tag{86}$$

To make x_o equal to x_i, this means:

$$\frac{K_f\big(G_r(s) + G_p(s)\big)}{\frac{1}{K_a G_v(s) G_c(s)} + K_f G_p(s)} = 1 \tag{87}$$

Then, the following equation can be calculated:

$$G_r(s) = \frac{1}{K_a K_f G_v(s) G_c(s)} \tag{88}$$

However, in reality, implementing Equation (88) is very difficult, especially when it is very complex. Therefore, it is often approximated as a first-order differential unit, which can elevate the control system to a second-order level. Therefore, Equation (88) can be changed to:

$$G_r(s) = \frac{1}{K_a K_f K_v K_c} s \tag{89}$$

where K_v is the molecular coefficient of $G_v(s)$ and $K_c(s)$ is the molecular coefficient of $G_c(s)$.

The compensation unit transfer function of the rotary joint system was obtained according to the above method and the results were compared with the system without feedforward compensation, as shown in Figure 16. The input signal is $x(t) = t$. The error can reach 0.45° without compensation, and after feedforward compensation, the error is less than 0.1°. It is apparent that feedforward compensation accelerates the response speed of the system and greatly reduces system error.

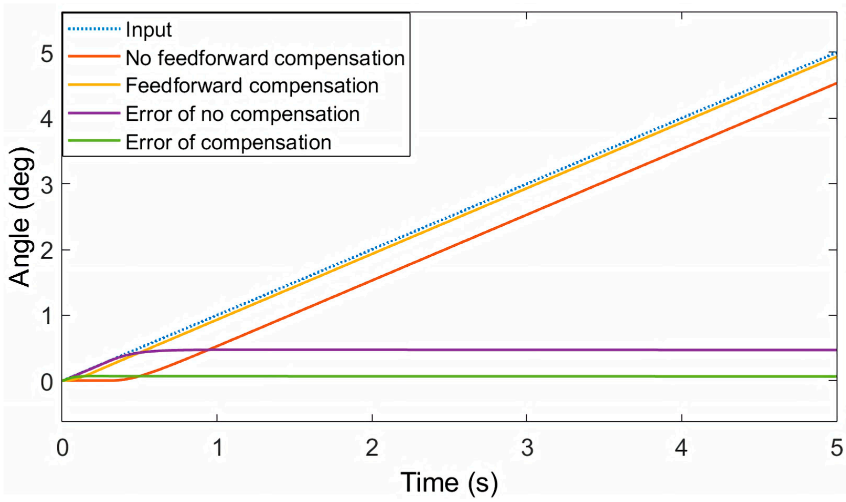

Figure 16. The effect of feedforward compensation under ramp input.

7. Results and Discussion

In this study, the wave period of the wind farm was 6 s, the significant wave height was set as 2.2 m, and the wave direction was 45°. The initial rotary joint angle and initial pitch joint angle were 0, and initial telescopic length was 0.5 m. In this case, the control effects of ordinary PID and fuzzy PID with feedforward compensation were compared.

The errors between the output angle and the expected angle of the ordinary PID and fuzzy PID algorithms are shown in Figure 17. In rotary joint control, the error of PID control was within (−0.66°, 0.65°), while the error for fuzzy PID control can be reduced to (−0.6°, 0.44°). In pitch joint control, ordinary PID control displays error within ±6°, while the error for fuzzy PID control can be reduced to (−4°, 5°).

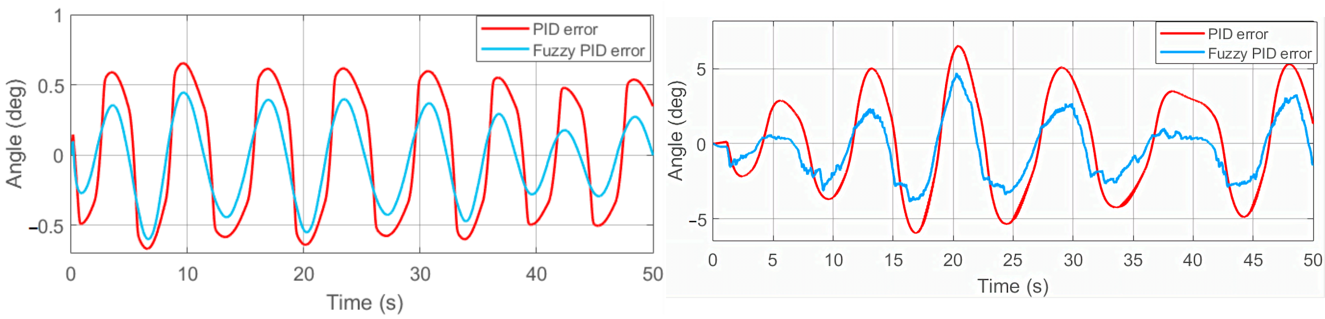

(**a**) (**b**)

Figure 17. Angle error comparison: (**a**) angle error of the rotary joint hydraulic cylinder and (**b**) angle error of the pitch joint hydraulic cylinder.

Figure 18 shows a comparison of the position error of the hydraulic cylinder of the ordinary PID and fuzzy PID algorithms. For rotary joint control, the position error of ordinary PID control was controlled within ±7 mm, while fuzzy PID control can reduce the error to (−6.4 mm, 4.8 mm). The error of the fuzzy PID was greater than the error of the PID in a short period of time. For pitch joint control, the error was controlled within

±160 mm by ordinary PID, while for fuzzy PID, the error was reduced to ±80 mm. In the control of the telescopic joint, the error displacement of ordinary PID control was within ±150 mm, while fuzzy PID control can reduce the error to (−100 mm, 80 mm). It is worth noting that Figures 17a and 18a are very similar, because the rotary joint uses a symmetrical hydraulic cylinder as the execution unit, and hydraulic valves, angle sensors, power amplifiers, etc., can be considered as proportional components.

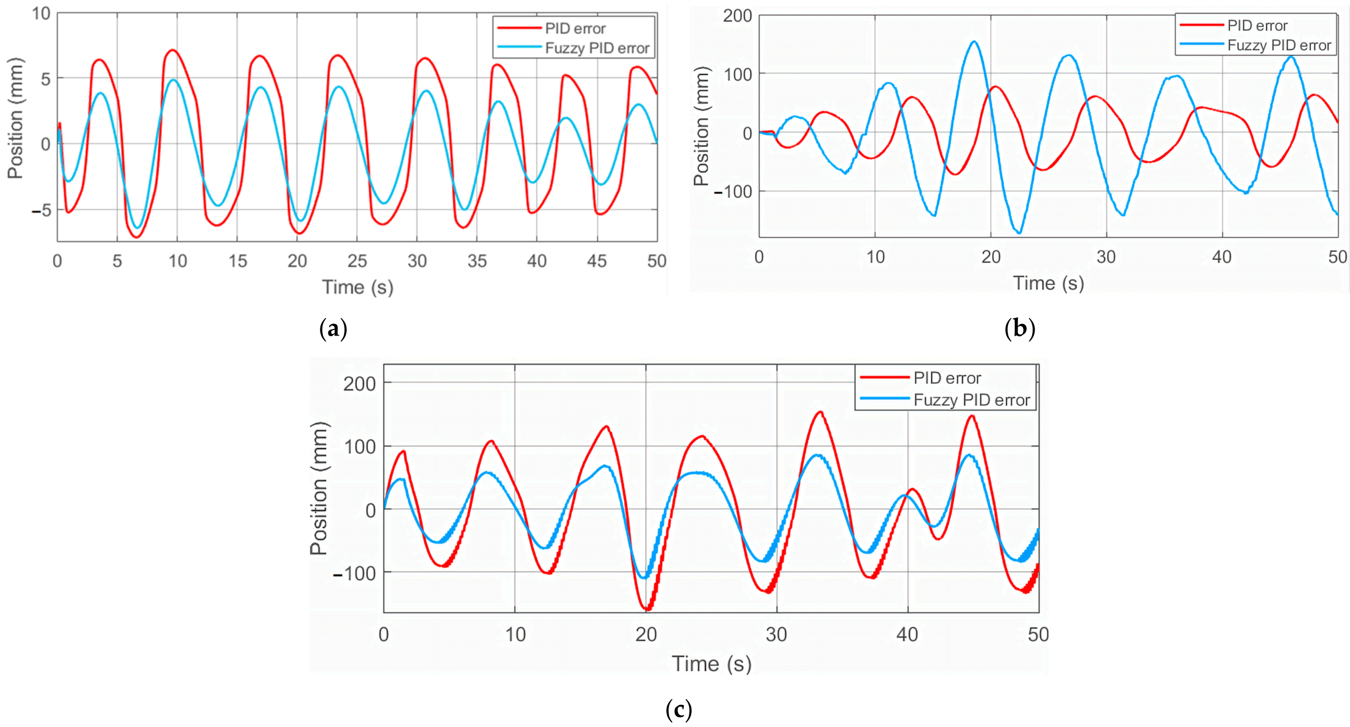

Figure 18. Position error comparison: (**a**) position error of the rotary joint hydraulic cylinder, (**b**) position error of the pitch joint hydraulic cylinder, and (**c**) position error of the telescopic joint hydraulic cylinder.

The position of the TAS end effector at the X-axis, Y-axis, and Z-axis after 50 s of simulation is shown in Figure 19. Before compensation, the maximum position error in the X direction can reach 0.2396 m, the maximum position error in the Y direction can reach 0.2032 m, and the maximum position error in the Z direction can reach 1.2907 m. However, it is obvious that the position error was greatly reduced whether using PID control or fuzzy PID control. For the former, the maximum error of displacement in the X direction was reduced to 0.0526 m, that in the Y direction was reduced to 0.1256 m, and that in the Z direction was reduced to 0.4805 m. For the latter, the maximum error of displacement in the X direction was reduced to 0.0441 m, that in the Y direction was reduced to 0.0967 m, and that in the Z direction was reduced to 0.3492 m.

The roll angle, pitch angle, and heave height were compared before and after compensation here. Since the TAS is not located on the roll and pitch axes, the roll and pitch angles defined here are different from those of the ship. In this study, the roll angle of the TAS, φ_t, is defined as: the angle between the projection of the line connecting the end of the TAS and the center of the B coordinate system in the plane with waves and the z-axis without waves. The pitch angle of the TAS, θ_t, is defined as: the angle between the projection of the line connecting the end of the TAS with and without waves on the y_0Bz_0 plane and the vertical plane, where the end of the TAS is located in the absence of waves. The vertical heave height of the TAS, z_t, is defined as the height difference between the end of the TAS with and without waves. The results calculated based on the above definition are shown in Figure 20.

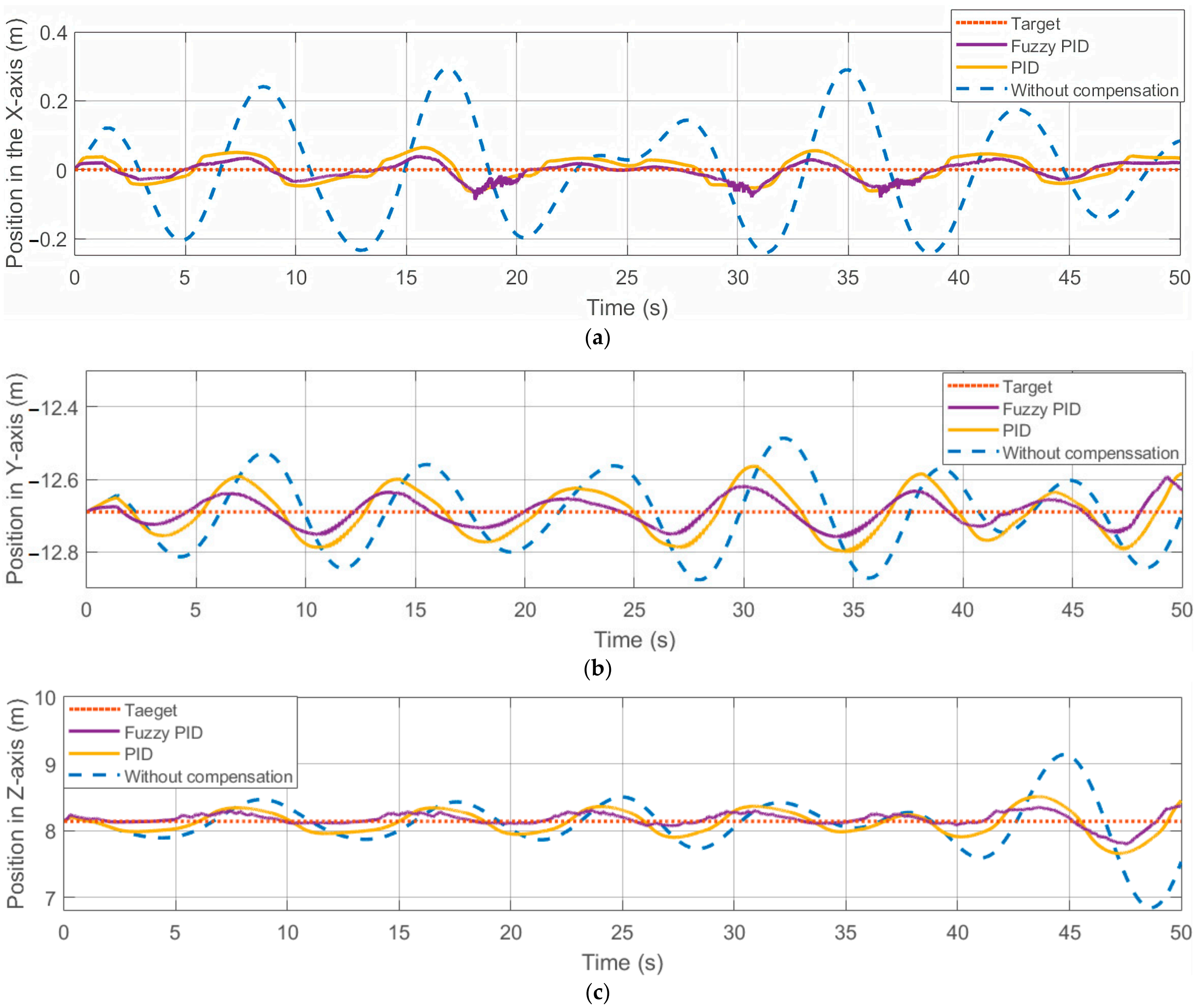

Figure 19. The compensation response at the TAS end effector when the encounter angle is 45 degrees. (**a**) The displacement in the X direction, (**b**) displacement in the Y direction, and (**c**) displacement in the Z direction.

The roll angle of the TAS under the action of waves was between (−2.76°, 4.74°) without compensation, and the difference between the highest and lowest amplitudes was 7.5°. After PID compensation, the roll angle was reduced to ±0.8°, with a reduction of 78.7%. After fuzzy PID compensation, the roll angle was reduced to 0.57°, with a reduction of 84.8%. For the pitch angle, θ_t, the pitch angle of the TAS was between (−0.08°, 0.056°) without compensation, and the difference between the highest and lowest amplitudes was 0.136°. Obviously, the amplitude of the pitch angle is very small compared to the ship's roll angle, due to the different definitions of the pitch angle. After PID compensation, the pitch angle decreased to ±0.022°, with a decrease of 67.6%. After fuzzy PID compensation, the pitch angle decreased to (−0.014°, 0.020°), with a reduction of 75%. For the heave height, z_t, the heave height of the TAS was between (−0.665 m, 0.549 m) without compensation, and the difference between the highest and lowest amplitudes was 1.214 m. After PID compensation, the heave height was reduced to (−0.297 m, 0.306 m), with a reduction of 50.3%. After fuzzy PID compensation (−0.106 m, 0.214 m), the reduction was 73.6%. Based on the above data comparison, fuzzy PID control can effectively reduce the roll angle, pitch angle, and heave height of the TAS, while maintaining end stability.

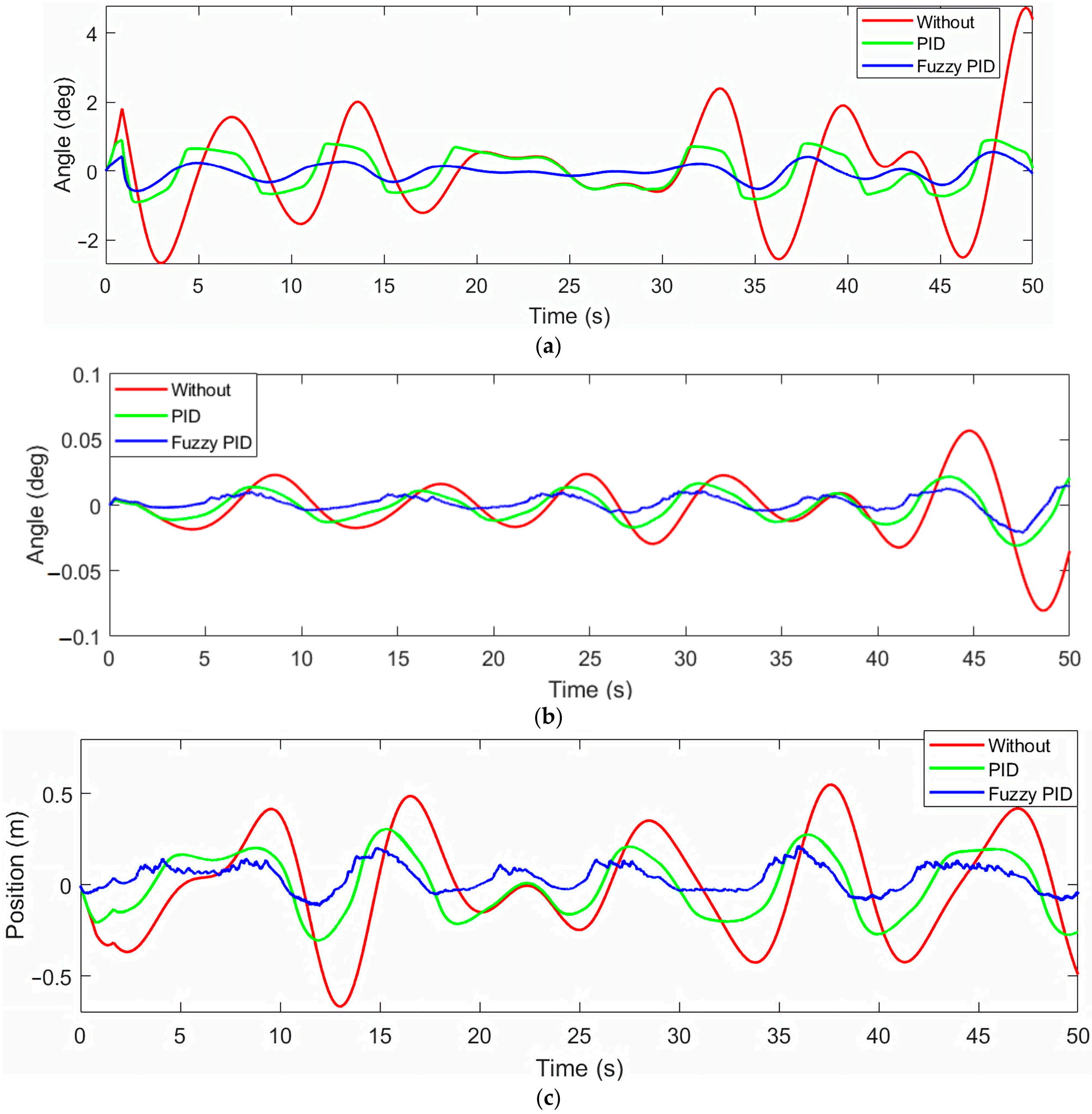

Figure 20. Roll angle, pitch angle, and heave height of the TAS when the encounter angle is 45 degrees. (**a**) Roll angle, (**b**) pitch angle, and (**c**) heave height.

In order to compare the results of the different control methods in more detail, the root mean square error (RMSE) was used to compare the error between the displacement and the ideal output displacement under different conditions to evaluate the performance of the control method. The RMSE formula can be described as:

$$RMSE = \sqrt{\frac{\sum_{i=1}^{n} (d - d_{tar})^2}{n}} \tag{90}$$

where d is displacement with or without compensation, d_{tar} is expected displacement, and n is the number of data points.

The calculation formula for compensation efficiency is as follows:

$$E = \frac{RMSE_{before} - RMSE_{after}}{RMSE_{before}} \tag{91}$$

where $RMSE_{before}$ is the RMSE without compensation, and $RMSE_{after}$ is the RMSE after compensation.

RSME in the X direction, Y direction, and Z direction was calculated without compensation, under PID control and fuzzy PID control. The compensation efficiency in each case was calculated, and the results are shown in Table 8. It is evident that the displacement error was greatly reduced after compensation whether in the X direction, Y direction, or Z direction. Without compensation, the displacement errors in three directions were 0.1039, 0.1226 m, and 0.3316 m, respectively. However, after PID compensation, the displacement errors were reduced to 0.0312 m, 0.0722 m, and 0.1843 m, respectively, and the compensation efficiency was 69.98%, 41.08%, and 44.44%, respectively. After fuzzy PID compensation, the displacement errors were reduced to 0.0180 m, 0.0429 m, and 0.0923 m, respectively. Fuzzy PID compensation can achieve a compensation efficiency of 82.69%, 65.03%, and 72.18% in three degrees of freedom, respectively. The stability of the TAS end effector has been greatly improved. There is no doubt that fuzzy PID control greatly increases the stability of the TAS end effector and has better performance than PID control. To sum up, fuzzy PID can effectively reduce the displacement error of the TAS end effector in the X, Y, and Z directions and enhance the stability of the TAS, and its result is better than that of PID control.

Table 8. RMSE and compensation efficiency in the X direction, Y direction, and Z direction.

Object	X	Y	Z
Without compensation, $RSME_1$ (m)	0.1039	0.1226	0.3316
Compensation with PID, $RSME_2$ (m)	0.0312	0.0722	0.1843
Compensation with fuzzy PID, $RSME_3$ (m)	0.0180	0.0429	0.0923
Compensation efficiency of PID, E_1	69.98%	41.08%	44.44%
Compensation efficiency of fuzzy PID, E_2	82.69%	65.03%	72.18%

In addition, the trajectory of the end effector can be obtained according to the displacement data of the end effector, and its trajectory is shown in Figure 21. The end effector shook violently before compensation, and the motion track seriously deviated from the target position. After PID compensation, the displacement error decreased a lot; that is, the range of the green line in the figure decreased a lot, which indicates that the compensation was effective. Finally, it is worth noting that the range of the track of fuzzy PID control, namely the magenta line, is closer to the target position, which indicates that the effect of fuzzy PID control is better than that of PID control.

When the encounter angle becomes 90, the situation becomes different. The roll, pitch, and heave heights of the TAS at this time are shown in Figure 22. For the roll angle, the size did not increase but decreased instead. The roll angle of the TAS before compensation was (−2.84°, 4.45°), and the difference between the highest and lowest amplitudes was 7.29°, which is 2.8% less than the obtained 7.5° when the encounter angle was 45 degrees. After PID compensation, the amplitude of the roll angle decreased to (−0.923°, 0.892°), with a decrease of 75.1%. After fuzzy PID compensation, the amplitude of the roll angle was reduced to (−0.684°, 0.452°), with a decrease of 84.4%. The decrease in amplitude was not significant compared to when the encounter angle was 45 degrees. For the pitch angle, the amplitude range of the pitch angle before compensation was (−0.075°, 0.071°), and the difference between the highest and lowest amplitudes was 0.136°, which is an 7.4% increase compared to the obtained 0.136° when the encounter angle was 45 degrees. After

PID compensation, the amplitude of the pitch angle decreased to (−0.035°, 0.029°). After fuzzy PID compensation, the amplitude of the pitch angle was reduced to (−0.024°, 0.019°). For the heave height, the range of heave height before compensation was 1.170 m, and the difference between the highest and lowest heave heights was 2.340 m, which is an increase of 89.4% compared to the obtained 1.214 m at an encounter angle of 45 degrees. After PID compensation, the heave height was reduced to (−0.516 m, 0.468 m). After fuzzy PID compensation, the heave height was reduced to (−0.37 m, 0.314 m). Overall, compared to an encounter angle of 45 degrees, the roll angle decreased, while the pitch angle and heave height increased. The reason for this is the same as in Figure 3. The change in the encounter angle to 90 degrees increased the roll angle and heave height of the ship, while the pitch angle decreased. However, in this case, the coordinate direction of the TAS is not consistent with the coordinate direction of the ship, but is 90 degrees different, which increases the ship's roll and causes an increase in the TAS pitch. The decrease in the ship's pitch angle leads to a decrease in the TAS roll angle. The direction of heave is the same, so the heave height increases.

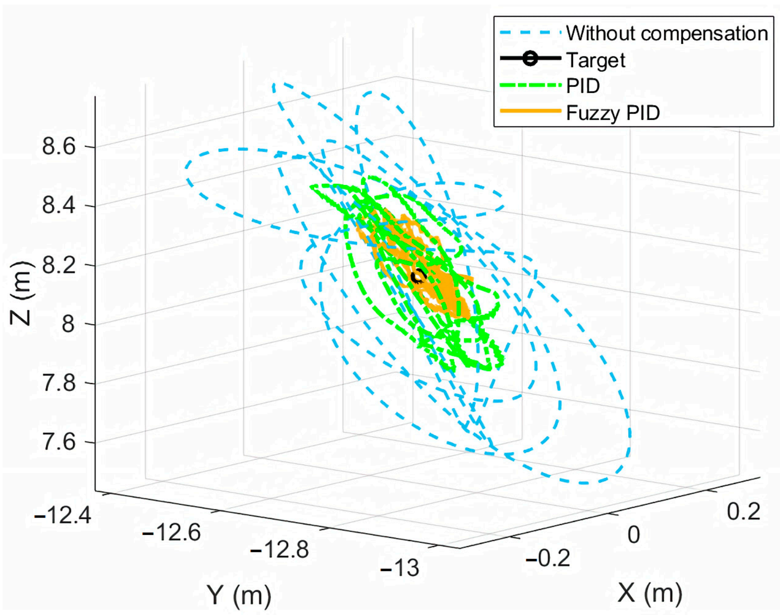

Figure 21. The motion trajectory of the end effector of the TAS.

For the position in the X, Y, and Z directions at an encounter angle of 90 degrees, the results are shown in Figure 23. Before compensation, the maximum position error in the X direction could reach 0.2173 m, the maximum position error in the Y direction could reach 0.2983 m, and the maximum position error in the Z direction could reach 1.4693 m. Obviously, compared to the encounter angle of 45 degrees, the displacement of the TAS on the X-axis was significantly reduced, while the displacement on the Y-axis and Z-axis significantly increased. This is because at the encounter angle of 90 degrees, the increase in ship roll angle increases the displacement of the TAS on the Y-axis and Z-axis, and the decrease in pitch reduces the displacement of the TAS on the X-axis.

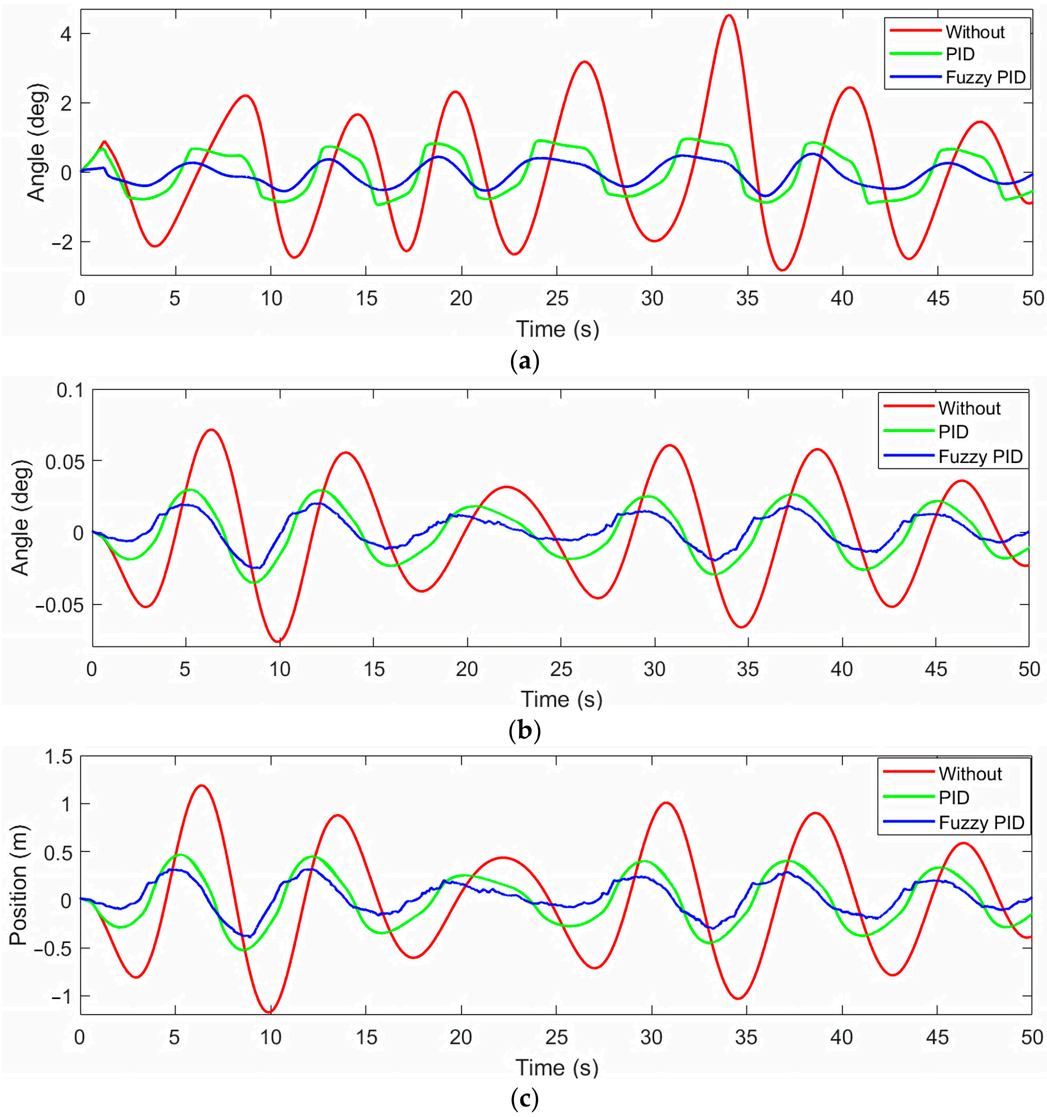

Figure 22. Roll angle, pitch angle, and heave height of the TAS when the encounter angle is 90 degrees. (**a**) Roll angle, (**b**) pitch angle, and (**c**) heave height.

Moreover, it is obvious that the position error was greatly reduced whether using PID or fuzzy PID control. For the former, the maximum error of displacement in the X direction was reduced to 0.0548 m, that in the Y direction was reduced to 0.1629 m, and that in the Z direction was reduced to 0.5596 m. For the latter, the maximum error of displacement in the X direction was reduced to 0.0447 m, that in the Y direction was reduced to 0.1183 m, and that in the Z direction was reduced to 0.4468 m. The changes in these data are also consistent with the above discussion.

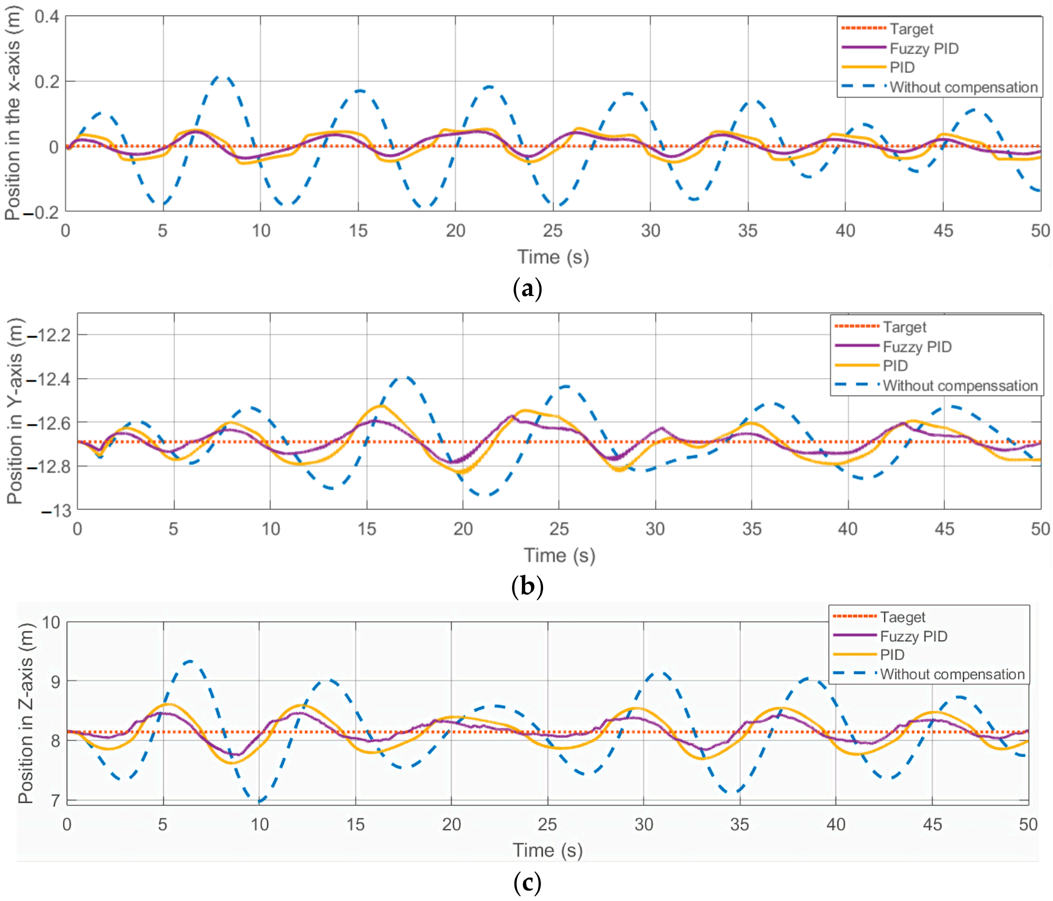

Figure 23. The compensation response at the TAS end effector when the encounter angle is 90 degrees. (**a**) The displacement in the X direction, (**b**) displacement in the Y direction, and (**c**) displacement in the Z direction.

8. Conclusions

A novel turbine access system for the Fujian coastal area was designed to solve the problem of the stability of the end of the TAS under sea conditions with a significant wave height of 2.2 m, including structural design, hydraulic drive design, and control system design. This study conducted the following work:

- A TAS was designed for the sea area near Putian City in Fujian Province, which includes a rotary joint, a pitch joint, and a telescopic joint. The specific compensation range was developed, and the specific length and weight of each joint were designed.
- The D-H parameter table of the TAS was obtained through the D-H parameters method, the kinematic model of the TAS was established, and the reachable motion space of the TAS was displayed; then, the 3-DOFs hydraulic control system model was determined.
- A new stacking compensation method was proposed to compensate for the roll angle, pitch angle, and heave height at the end of the TAS. The effects of ship roll, pitch, and heave on the end of the TAS were analyzed separately and compensation values were calculated. The sum of the compensation values was used as the final compensation value for the TAS.
- A fuzzy PID controller with feedforward compensation was designed and a simulation diagram was built in MATLAB/Simulink to test the feasibility of the design, and then compared with the simulation results of PID. The experimental results showed that the fuzzy PID control with feedforward compensation can achieve maximum compensation efficiencies of 84.8%, 75%, and 73.6% for the roll angle, pitch angle, and heave height of the TAS, respectively, all higher than the 78.7%, 67.6%, and 50.3% achieved under PID control. In addition, the former algorithm can achieve a

maximum compensation efficiency of 82.69% on the X-axis, much higher than the 69.98% achieved using PID control.

Moreover, this study achieved good results in roll angle compensation and pitch angle compensation, which can make the error of the TAS end in the X-axis and Y-axis less than 15 cm. However, the error in the heave direction is still relatively large, ranging from 0.3 m to 0.4 m. Thus, it is necessary to explore new algorithms for heave compensation. In addition, the compensation strategy is subject to physical experiments, and future practical experiments are needed to further verify the effectiveness of the method.

Author Contributions: Conceptualization, J.W., S.Z. and Y.L.; methodology, J.W. and Y.L.; software, Y.L., S.Z., Y.S. and Z.W.; validation, Y.L. and J.W.; formal analysis, Y.L. and Y.S.; investigation, Y.L. and Z.W.; resources, J.W., S.Z. and J.C.; data curation, Y.L.; writing—original draft preparation, Y.L.; writing—review and editing, J.W. and Y.L.; visualization, Y.L. and Y.S.; supervision, J.W. and J.C.; project administration, J.W. and Y.L.; funding acquisition, J.W., Y.L., Y.S. and Z.W. All authors have read and agreed to the published version of the manuscript.

Funding: This work was partially supported by the National Natural Science Foundation of China (Grant No. 51875113) and the International Exchange Program of Harbin Engineering University for Innovation-oriented Talents Cultivation.

Institutional Review Board Statement: Not applicable.

Informed Consent Statement: Not applicable.

Data Availability Statement: The data used to support the findings of this study are included within the article and are also available from the corresponding authors upon request.

Conflicts of Interest: The authors declare no conflict of interest.

References

1. Zhang, J.; Wang, H. Development of offshore wind power and foundation technology for offshore wind turbines in China. *Ocean Eng.* **2022**, *266*, 113256. [CrossRef]
2. Faraggiana, E.; Sirigu, M.; Ghigo, A. Conceptual design and optimisation of a novel hybrid device for capturing offshore wind and wave energy. *J. Ocean Eng. Mar. Energy* **2023**, 1–22. [CrossRef]
3. Tang, G.; Lei, J.; Li, F. A modified 6-DOF hybrid serial–parallel platform for ship wave compensation. *Ocean Eng.* **2023**, *280*, 114336. [CrossRef]
4. Wei, Y.; Wang, A.; Han, H. Ocean wave active compensation analysis of inverse kinematics for hybrid boarding system based on fuzzy algorithm. *Ocean Eng.* **2019**, *182*, 577–583. [CrossRef]
5. Cerda Salzmann, D.J. Ampelmann: Development of the Access System for Offshore Wind Turbines. Ph.D. Thesis, Delft University of Technology, Delft, The Netherlands, 2010.
6. Fan, Q.; Wang, X.; Yuan, J. A review of the development of key technologies for offshore wind power in China. *J. Mar. Sci. Eng.* **2022**, *10*, 929. [CrossRef]
7. Hu, B.; Yung, C. Offshore Wind Access Report 2020. Available online: http://resolver.tudelft.nl/uuid:d6cefbf6-2916-42fc-bb3d-b2d713938e09 (accessed on 14 November 2023).
8. Ren, Z.; Verma, A.S.; Li, Y. Offshore wind turbine operations and maintenance: A state-of-the-art review. *Renew. Sustain. Energy Rev.* **2021**, *144*, 110886. [CrossRef]
9. Dai, L.; Stålhane, M.; Utne, I.B. Routing and scheduling of maintenance fleet for offshore wind farms. *Wind. Eng.* **2015**, *39*, 15–30. [CrossRef]
10. Acanfora, M.; Montewka, J.; Hinz, T. On the estimation of the design loads on container stacks due to excessive acceleration in adverse weather conditions. *Mar. Struct.* **2017**, *53*, 105–123. [CrossRef]
11. Southerland, A. Mechanical systems for ocean engineering. *Nav. Eng. J.* **1970**, *82*, 63–74. [CrossRef]
12. Yang, W.; Zhang, Z.; Zhang, A. Research on an active heave compensation system for remotely operated vehicle. In Proceedings of the 2008 International Conference on Intelligent Computation Technology and Automation (ICICTA), Changsha, China, 20–22 October 2008; pp. 407–410.
13. Küchler, S.; Sawodny, O. Nonlinear control of an active heave compensation system with time-delay. In Proceedings of the 2010 IEEE International Conference on Control Applications, Yokohama, Japan, 8–10 September 2010; pp. 1313–1318.
14. Huang, X.; Wang, J.; Xu, Y. Dynamic modeling and analysis of wave compensation system based on floating crane in smart port. In Proceedings of the 2018 International Symposium in Sensing and Instrumentation in IoT Era (ISSI), Shanghai, China, 6–7 September 2018; pp. 1–5.
15. Zhou, M.; Wang, Y.; Wu, H. Control design of the wave compensation system based on the genetic PID algorithm. *Adv. Mater. Sci. Eng.* **2019**, *2019*, 2152914. [CrossRef]

16. Xie, T.; Huang, L.; Guo, Y. Modeling and simulation analysis of active heave compensation control system for electric-driven marine winch under excitation of irregular waves. *Meas. Control* **2022**, *56*, 1004–1015. [CrossRef]
17. Christopher, N. Offshore Access Systems. U.S. Patent 5074382, 24 December 1991.
18. Rong, B.; Rui, X.; Lu, K. Dynamics analysis and wave compensation control design of ship's seaborne supply by discrete time transfer matrix method of multibody system. *Mech. Syst. Signal Process.* **2019**, *128*, 50–68. [CrossRef]
19. Tang, G.; Lu, P.; Hu, X. Control system research in wave compensation based on particle swarm optimization. *Sci. Rep.* **2021**, *11*, 15316. [CrossRef]
20. Cai, Y.; Zheng, S.; Liu, W. Sliding-mode control of ship-mounted Stewart platforms for wave compensation using velocity feedforward. *Ocean Eng.* **2021**, *236*, 109477. [CrossRef]
21. Yin, R.; Xie, W.; Wen, Y. Robust wave compensation controller design for an active hexapod platform with time-varying input delays. *Ocean Eng.* **2023**, *274*, 114084. [CrossRef]
22. Chen, W.; Wang, S.; Li, J. An ADRC-based triple-loop control strategy of ship-mounted Stewart platform for six-DOF wave compensation. *Mech. Mach. Theory* **2023**, *184*, 105289. [CrossRef]
23. Lan, Z.; An, C.; Yi, D. Multivariable fuzzy genetic controller for stabilized platform. In Proceedings of the 2015 34th Chinese Control Conference (CCC), Hangzhou, China, 28–30 July 2015; pp. 783–788.
24. Bai, X.; Turner, J.; Junkins, J. Dynamic analysis and control of a stewart platform using a novel automatic differentiation method. In Proceedings of the AAS Astrodynamics Specialist Conference and Exhibit, Keystone, Colorado, 21–24 August 2006; p. 6286.
25. Liu, J.; Chen, X. Adaptive control based on neural network and beetle antennae search algorithm for an active heave compensation system. *Int. J. Control Autom. Syst.* **2022**, *20*, 515–525. [CrossRef]
26. Chen, B.; Chiang, M. Simulation and experiment of a turbine access system with three-axial active motion compensation. *Ocean Eng.* **2019**, *176*, 8–19. [CrossRef]
27. Huang, Y.; Lin, C.; Chiang, H. Development of an Offshore Turbine Access System with Four-Axial Active Motion Compensation. In Proceedings of the 2022 8th International Conference on Applied System Innovation (ICASI), Nantou, Taiwan, 21–23 April 2022; pp. 127–129.
28. Tang, L.; Chen, Y. Dynamic model of four degree of freedom rope-driven rigid-flexible hybrid wave compensation device. *J. Mech. Sci. Technol.* **2020**, *34*, 1937–1948. [CrossRef]
29. Ampelmann. Available online: http://www.ampelmann.nl/products/e-type/ (accessed on 14 November 2023).
30. Houlder. TAS Steps up to Turbine Access Challenge—Houlder. Available online: https://www.houlderltd.com/tas-turbine-access-system-steps-access-challenge/ (accessed on 14 November 2023).
31. Zhang, B.; Wang, Y. Semi-submersible offshore coupled motion in irregular waves. *J. Marine Sci.* **2020**, *2*, 19–23. [CrossRef]
32. Yang, Z. Statistical properties and spectral analysis of wind waves. *Hydro-Sci. Eng.* **1985**, *3*, 81–98.
33. Guo, J.; Li, G.; Li, B. A ship active vibration isolation system based on a novel 5-DOF parallel mechanism. In Proceedings of the 2014 IEEE International Conference on Information and Automation (ICIA), Hailar, China, 28–30 July 2014; pp. 800–805.
34. Shi, J.; Zheng, J.; Zhang, C. A 39-year high resolution wave hindcast for the Chinese coast: Model validation and wave climate analysis. *Ocean Eng.* **2019**, *183*, 224–235. [CrossRef]
35. Fossen, T.; Perez, T. Marine Systems Simulator (MSS). Available online: https://github.com/cybergalactic/MSS (accessed on 14 November 2023).
36. Li, Y.; Zheng, J. The design of ship formation based on a novel disturbance rejection control. *Int. J. Control Autom.* **2018**, *16*, 1833–1839. [CrossRef]